11-15-2021

Low Gravity Natural Convection and Pool Boiling Predictions

Ashley Carol Milligan

LOW GRAVITY NATURAL CONVECTION AND POOL BOILING PREDICTIONS

by

Ashley Carol Milligan

A Thesis

Submitted in Partial Fulfillment of the

Requirements for the Degree of

Master of Science

Major: Mechanical Engineering

The University of Memphis

December 2021

Acknowledgements

I would like to thank my advisor, Dr. Jeffrey Marchetta, for his help and guidance throughout my time at the University of Memphis. I am very grateful to the Herff College of Engineering and the Department of Mechanical Engineering for funding this research. On a personal note, I want to thank my fiancé, Drew Austell, and my family and friends. I would not have made it through graduate school without their continuous love and support.

Abstract

Cryogenic fluids are used in various fields, such as biomedical technology, food transportation, and aerospace. Liquid hydrogen and oxygen are cryogenic fluids that can act as energy-dense fuels for long-term, large payload space flight. Much of the resulting research in long-duration cryogenic fluid storage has focused on zero-boil-off tank pressure control in low gravity environments. The high cost of testing these systems in low gravity has created a need to develop accurate models of the behavior of fluids in these environments. Simulations of tank pressure control require accurate models of evaporation and condensation phase change. Recent advancements in commercial fluid dynamics (CFD) simulation software offer potential to evaluate evaporation and condensation phase change models in low gravity two phase flows. The goal of this research is to use ANSYS FLUENT, a commercial CFD software, to simulate pool boiling in low gravity. The volume of fluid approach with the Lee phase change model, which predicts heat and mass transfer at the liquid vapor interface, has been recently added to FLUENT. Predictions of low gravity natural convection and nucleate pool boiling using FLUENT are presented and are compared to experimental data and previously published numerical simulations.

Table of Contents

List of Tables

List of Figures

Nomenclature

c_p = specific heat (J/kg K)

D = diameter (m or mm)

$\vec{F}$ = external body forces

E = total energy

g = gravitational acceleration (m/s²)

g_e = gravitational acceleration at sea level, 9.81 m/s²

h = heat transfer coefficient (W/m² K)

k = thermal conductivity (W/m K)

L = characteristic length scale (m)

$\dot{m}$ = mass transfer rate

Nu = Nusselt number

q = heat flux (W/m²)

Ra = Rayleigh Number

r_i = mass transfer intensity factor

S_m = source – mass added

t = time (s)

T = temperature (K or °C)

T_{bulk} = temperature of the bulk liquid

T_{sat} = saturation temperature at the given pressure

T_{wall} = temperature of the hot wall

ΔT_w = wall superheat, $T_{wall} - T_{sat}$

ΔT_{sub} = liquid subcooling, $T_{sat} - T_{bulk}$

U = internal energy

V or v = velocity

W = width of the cavity

α = thermal diffusivity (m²/s) or volume fraction

β = volumetric expansion coefficient (1/K)

μ = dynamic viscosity (

ρ = density (kg/m^3)

$\rho\vec{g}$ = gravitational body force

σ = surface tension (N/m)

$\bar{\bar{\tau}}$ = stress tensor

ν = kinematic viscosity (m^2/s)

ω = volume fraction

Subscripts:

v = vapor phase

l = liquid phase

1. Introduction

Systems involving substances at temperatures below -150°C (-238°F) are referred to as cryogenics. There are many cryogenic fluids that are liquids at these extreme temperatures, such as liquid hydrogen, oxygen, and nitrogen. Many industries utilize cryogenic fluids for a variety of purposes, such as food storage, chemical reactors, and rocket propellant [1].

There are many uses for cryogenics specifically in space applications. While using fluids such as liquid hydrogen or liquid oxygen for rocket propellants is the most well-known application in this industry, it is becoming more common to see research geared towards the use of cryogenics in low temperature storage and life support systems. Nevertheless, cryogenic propellants have remained an area of interest due to their high specific impulse when compared to solid propellants. In propulsion, higher specific impulse fuels are more efficient, meaning that they produce a greater amount of energy with the same mass of fuel [2]. Therefore, cryogenic fuels have a lower mass to store and launch for the amount of energy they can produce compared to solid fuels, which make them an ideal candidate for rocket propellant.

With the increasing interest in deep space travel and long-term manned missions, cryogenic fuel storage has become a growing research field [3]. Effective tank design is crucial to prevent propellant loss due to boiling over long-term missions. A prototype of a SpaceX liquid oxygen fuel tank is shown in figure 1. Design and testing of large-scale cryogenic fluid storage tanks in low gravity would be exceedingly expensive and time consuming. Thus, further design and development of cryogenic propellant management systems necessitates accurate models of cryogenic propellant fluid-thermal behavior in low gravity. In particular, a robust simulation of low gravity boiling of cryogenic fluids is needed to further develop a useful large-scale zero-boil-off tank.

Figure 1: SpaceX liquid oxygen fuel tank prototype for manned Mars missions aboard the Interplanetary Transport System [4]

Researchers have been developing correlations and numerical simulations for pool nucleate boiling since the 1950s [5]. Multiple theoretical and computational models of varying complexity have been developed to simulate tank pressurization behavior, but are inconsistent when compared to experimental data [6]. Simulations of tank pressure control require accurate physics models, including evaporation and condensation phase change in low gravity. Recently, numerical simulations have been created that can simulate natural convection, nucleate pool boiling, and bubble growth and departure in microgravity with great accuracy compared to experiments [7–9]. These simulations are often complex and require a great knowledge of programming and computational fluid dynamics (CFD). However, recently developed models of evaporation and condensation have been added to commercial CFD software that may enable accurate simulation of low gravity natural convection and pool boiling [10–12]. This work aims to assess whether these recently added evaporation and condensation models can be used to

accurately model pool boiling in low gravity. Simulations for natural convection and pool boiling in low gravity are conducted and compared to experiment data.

1.1 Literature review

1.1.1 Cryogenic Liquid Storage

Some of the earliest research in low gravity and cryogenic fluid storage was conducted by researchers at the NASA Lewis Research Center. Aydelott et al. performed a series of experiments investigating self-pressurization of liquid hydrogen tanks. The variables studied included heating method and rate, gravity, tank size, percent of tank filled, temperature, and pressure.. Results show that the heating location (top, bottom, or uniform) had the largest impact on rate of pressure rise, and that evaporation was most present in the uniform and top heating tests [13]. Gravity effects on tank self-pressurization were also studied by Aydelott. Specifically, spherical tanks filled with liquid hydrogen were evaluated. When compared to earth-gravity cases, the low gravity cases had a substantially lower pressure rise rate. It was determined that this was largely due to an increase in both wetted wall area and boiling, and the greatest variable in determining these quantities was the location of the heat source [14]. Normal gravity experiments were performed to evaluate the effect of tank size on pressure rise. The researchers were able to predict pressure rise by using a relationship involving heat transfer per unit volume, but noticed a difference in homogeneity of the fluid in different tank sizes due to the wall thickness [15].

Further research in improved tank design often focuses on active and passive technologies to decrease boiling. Active technology in this scenario is most often the use of an active cryogenic refrigerator (cryocooler) (Kittel et al., 2002). However, active systems require power which is

limited on spacecraft. Passive technologies consist of additions such as vapor-cooled shields, sunshades, and improved tank insulation (Plachta et al., 2006).

Salerno and Kittel [3] provide an in-depth description of cryogenic technology and various methods for zero gravity cryogenic fluid management. Active and passive cooling designs are discussed, as well as the promising optimization of a hybrid cooling approach. Cryogenic tanks with different requirements, such as size, fluid, and temperature, were planned to be tested for optimization in Mars missions in the 2010s, but the study has yet to be completed. As part of the experiment plan, cryogenic storage requirements were developed for the Mars mission. These requirements include different operating environments, such as launch from earth, ascent to the surface of Mars, storage on the surface, and different temperature conditions to be evaluated at each case.

While tank designs are improving and some studies have shown that zero boil-off tanks can be achieved deeper in space [16], the ability to validate each new improvement is still extremely expensive and time intensive. Reliable computational simulations provide researchers and tank designers the ability to perform tests on multiple tank designs before investing in full low gravity experimental tests.

1.1.2 Low Gravity Experiments

Experiments regarding low-gravity boiling heat transfer were first performed in the 1960's. Siegel and Keshock [17] conducted NASA-sponsored experiments which utilized drop towers and lasted only a few seconds. The studies involved electrically heated wires in freefall and evaluated bubble growth and departure. Distilled water, liquid nitrogen, and alcohol were all studied. The liquids were saturated and on horizontal, heated wires and ribbons. The boiling

curve did not appear to be greatly affected by change in gravity level. Longer duration low gravity experiments involving magnetic particles were carried out by Papell and Faber [18]. These experiments utilized magnetic body forces to counteract the influence of Earth gravity on a colloidal magnetic fluid. They were able to achieve a steady-state boiling curve, which showed a decrease in wall superheat when gravity changed from earth gravity to microgravity. These and other studies in the 1960s often contradicted each other when comparing the effect of gravity on heat transfer, likely due to the short length of each experiment, but often resulted in similar visual findings [19]. From early on one of the key visual qualities of low gravity boiling was the formation of one large bubble, as seen in figure 2. This finding has been present in studies from the 1960s and continues in the most recent low gravity boiling experiments.

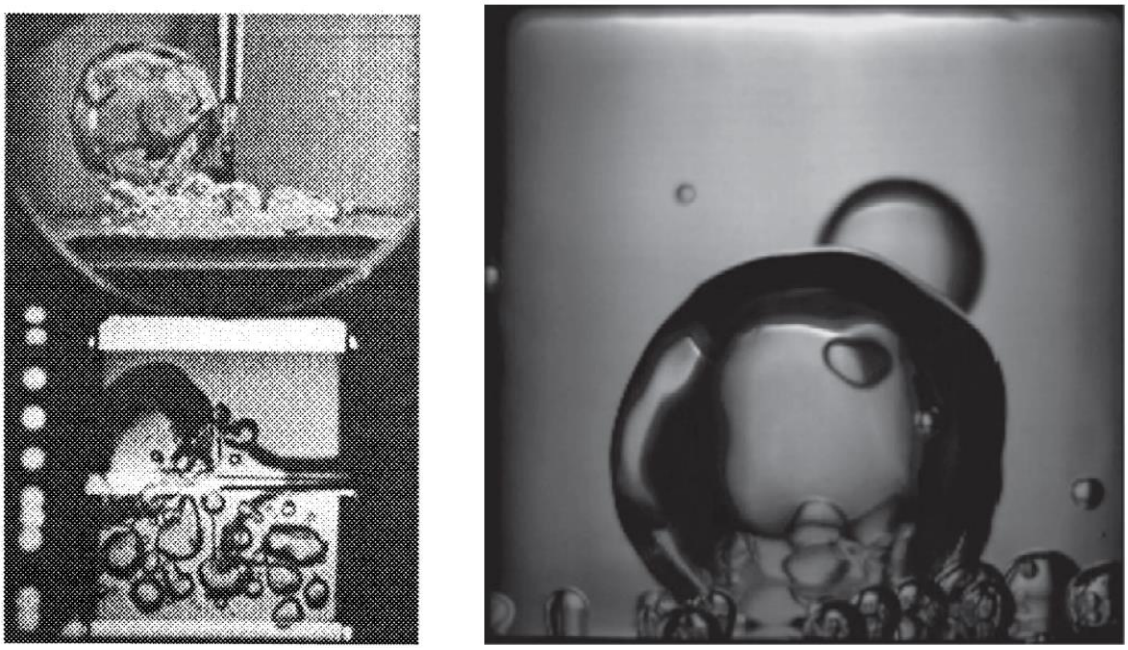

(a) **(b)**

Figure 2: (a) Bubble formation from experiments by Merte et al. [20]
(b) Visual data captured in the Nucleate Pool Boiling Experiments on the ISS. This bubble was captured at a flow time of 410 seconds [7].

Pool boiling experiments were performed on the International Space Station (ISS) by Merte, Lee, and Keller [20,21] in the 1990's aboard the space shuttle. The fluid analyzed was the fluorocarbon R-113. The experiments studied pool boiling at steady state by varying the heat flux and liquid subcooling. Bubble formation and growth was observed in many cases, and pool boiling curves for R-113 were created for two levels of subcooling.

Raj, Kim, and McQuillen performed experiments in the Boiling Experimental Facility (BXF) on the ISS during March – May of 2011 [22]. A picture of the BXF is shown in figure 3. The Microheater Array Boiling Experiment (MABE) was one of two experiments within the BXF. The experiment evaluated many boiling characteristics in low gravity, such as the onset of nucleate boiling and the effect of subcooling and pressure. The researchers found that as pressure increased, the superheat needed for nucleate boiling to begin decreased, but in low gravity when nucleate boiling occurred, smaller superheats were needed compared to tests performed in earth gravity. Heat flux values at lower superheats are shown to be greater than they would be in earth gravity environments. They also found that heat transfer rates were proportional to liquid subcooling and pressure.

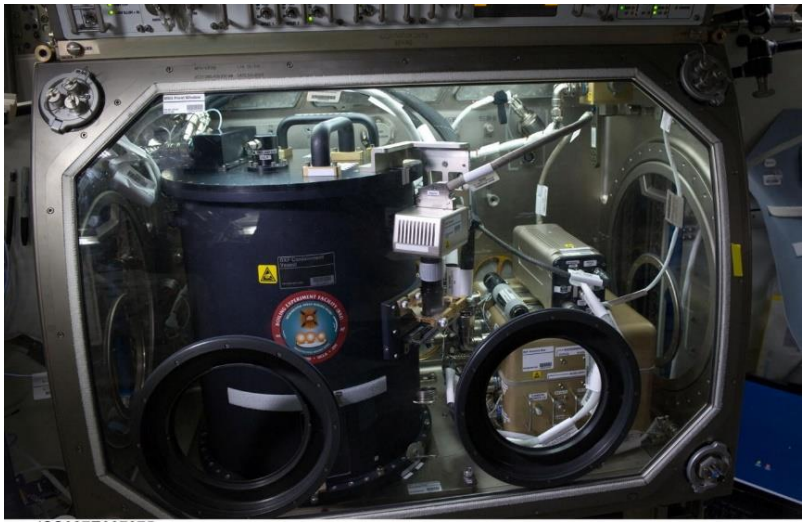

Figure 3: The Boiling Experimental Facility on the ISS [7]

The second experiment housed in the BXF was the Nucleate Pool Boiling Experiment (NPBX) by Warrier et al. [7]. In this experiment, the test chamber was filled with perfluoro-n-hexane and maintained at a constant pressure with the use of bellows. The fluid was initially at a constant bulk temperature, and an 89.5 mm aluminum wafer was heated from the underside. Experiments were performed to obtain data for natural convection, nucleate pool boiling, and bubble dynamics. The results compared favorably with previous experiments and numerical correlations. The data from this experiment has been used to create numerical models and is discussed in greater detail in later sections.

1.1.3 Computational Studies

The first widely accepted multiphase models were first published in the 1980s. The LaGrangian method published by Ryskin and Leal [23] simulates a buoyancy-driven flow with a rising deformable bubble in a 2-dimensional axisymmetric domain. The model tracks individual particles within the flow, making it very computationally intensive and not ideal when applied to more complex 3-dimensional flows. The level-set method [24] defines the distance from the interface implicitly. This method is commonly used in simulations due to its ability to capture more complicated geometries and surfaces. One of the downfalls of this method is the inability for phase change to occur anywhere other than the interface. This method is used often by Dhir and coworkers in various models that will be discussed in later sections. The volume of fluid (VOF) method [25] was published in 1981 and has also been used in many models. This model is one of the few multiphase models contained within FLUENT and is the basis for the research herein.

The earliest phase change models came to prominence in the 1950s. Since then, models have become more complex and have been combined with other models used to simulate fluid flow, largely due to increased computational ability. One of the earliest phase change models is the Schrage model [26], which is based on the kinetic theory of gases. This model calculates phase change using the flux between particles crossing the liquid-vapor interface. The energy jump model [27] bases mass transfer rate on the transfer of energy across the interface based on the Rankine-Hugoniot jump condition. While both the energy jump and Schrage models are commonly used for nucleate pool boiling in the literature [28], neither are available in FLUENT. The Lee model [29] is a respected phase change model that is a new addition to FLUENT as way to simulate evaporation and condensation within the Volume of Fluid multiphase model. This semi-implicit numerical scheme calculates the volume fraction inside the pressure iteration loop using the mass and momentum equations for each individual phase. This model has shown to be stable and converges quickly. It is used in the present study and will be discussed in greater detail in the methods section.

Studies have also been conducted to assess the validity of evaporation models for cryogenic fluid evaporation. Midha et al. found that the CFD tool FLACS has accurately predicted hydrogen gas dispersion from liquid hydrogen spills [30]. Nawaz et al. analyzed six evaporation models, and found that they all over-predicted the vaporized liquid mass [31]. Multiple theoretical and computational models of varying complexity have been developed to simulate tank pressurization behavior, but are inconsistent compared to one other and experimental data [6].

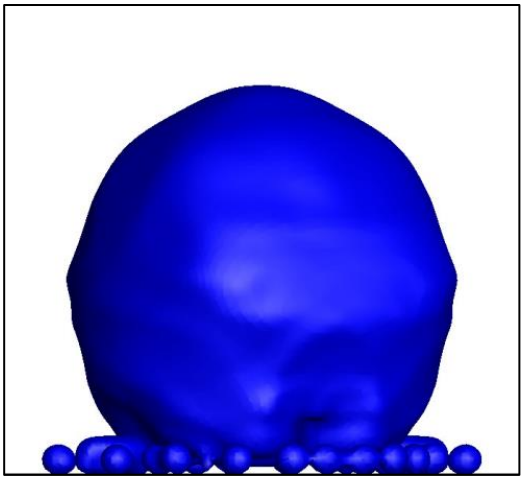

Figure 4: A bubble produced from a low-gravity numerical simulation of pool boiling [8]

Experimental data from the two experiments from the BXF were used to verify models created by researchers from the two groups. The model by Raj et al. consisted of a gravity scaling parameter for heat flux that was developed based on earlier parabolic flight data and was then updated based on data from the Microheater Array Boiling Experiment (MABE). This updated model predicted the low gravity experimental data, specifically heat flux, within ± 20% [22]. Models by Aktinol and Dhir [8] were able to recreate the bubble formation, departure, and growth in low gravity. Figure 4 shows simulated results from one of the tests. These models consist of a 2-dimensional axisymmetric domain with a finite difference scheme. A level set method is used to track the interface between the two phases, and the solid and fluid interface is tracked. The researchers coupled the solid heater with the simulation and applied a heat flux across the solid to simulate the hot wall as opposed to assuming a constant surface temperature like many previous models. The domain is split into a micro and macro region in order to capture both the thin film that forms underneath the bubbles and the bulk fluid behavior. The model assumed the flow is laminar and that the fluid and solid properties are constant.

1.2 Background

1.2.1 Basics of Boiling

Flow and pool boiling are the two main types of boiling. Flow boiling involves fluid flowing across a heated surface, such as a hot plate or inside a duct. The flow is forced to move by an outside force such as a fan, pump, or gravity, and heat is predominately transferred through forced convection. Pool boiling is likely more familiar to a general audience. In pool boiling, a pool of fluid is heated from a superheated wall, and any movement of the fluid is caused by a change in density. The most common example of pool boiling is a pot of water on a hot eye of a stove. For the applications examined in the present research, pool boiling will be examined.

1.2.2 The Boiling Curve

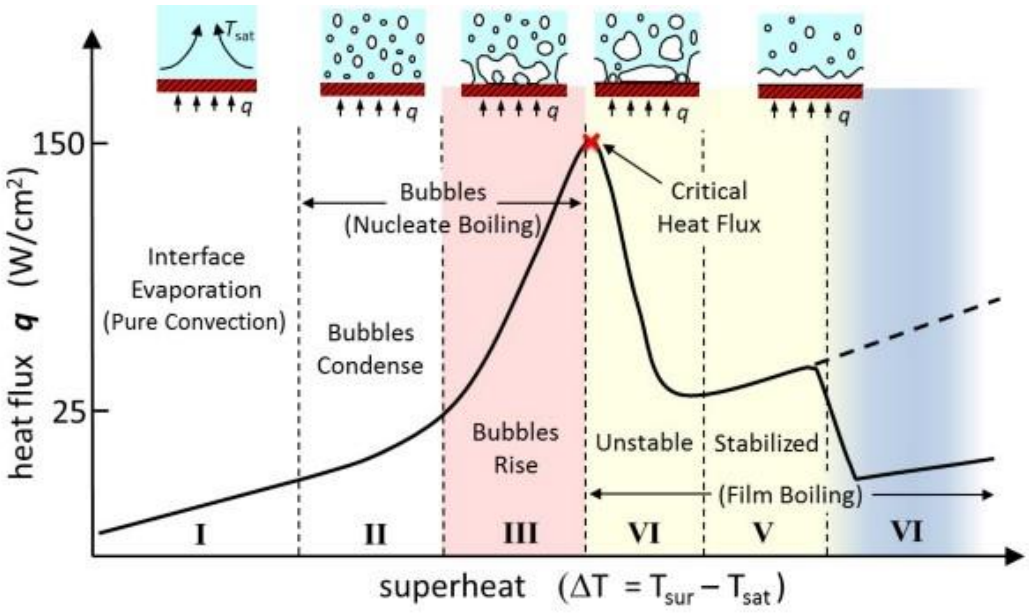

Figure 5: The Boiling Curve [32]

Pool boiling occurs in various stages, or regimes. The bulk pool of fluid is initially at a set temperature, called the bulk temperature herein. This bulk temperature is typically less than or equal to the saturation temperature of the fluid at the system pressure. Once a wall, often the bottom of the bulk fluid container, is set to a different temperature, the boiling regime can be examined. Wall superheat is defined as the difference between the wall temperature and the saturation temperature of the fluid. Figure 5 shows a typical boiling curve for liquid water. The exact quantitative values where each regime occurs vary from fluid to fluid, but the general curve is consistent for most fluids. Each wall superheat corresponds with a value for heat flux once quasi-steady state conditions have been reached. In the literature and present work, the fluid is considered to be at quasi steady state once at least 10 seconds have passed with constant wall heat flux and vapor volume.

In cases where the wall superheat is negative (wall temperature is less than the saturation temperature) natural, or pure, convection occurs. This is shown as regime I on figure 5. Natural convection is when fluid movement and convective heat transfer occurs due to changes in fluid density from temperature.

If the wall superheat is greater than zero, boiling will begin to occur. There are two main types of boiling within pool boiling: nucleate boiling and film boiling. As the wall superheat increases, the boiling regimes will transition from nucleate to film boiling. The first stage once boiling begins, regime II in figure 5, consists of small bubbles beginning to condense. The next regime in nucleate boiling is when bubbles begin to rise and occurs until the fluid reaches the critical heat flux. This point, shown between regimes III and IV on figure 5, is where flow transition begins and switches to film boiling. Film boiling occurs where a thin film of vapor is present between the bulk fluid and the heated wall, as shown in figure 5. Film boiling is much

more unstable and unpredictable than nucleate boiling. For the present study, only natural convection and nucleate boiling (regimes I, II, and III) are considered.

Natural convection/Stefan problems

To validate the ability for the commercial software to predict and model low gravity pool boiling, it is first necessary to verify that the software can accurately simulate natural convection at different levels of gravity. This is done by analyzing a variation of a common boundary value problem, the Stefan Problem. The type of Stefan problems evaluated in this work involve differentially heated walls on either side of the domain.

In flows consisting of only natural convection, the intensity of the buoyancy-driven flow is described using the Rayleigh number, Ra.

$$\mathrm{Ra} = \frac{g\beta(T_{wall}-T_{bulk})L^3}{\upsilon\alpha} \quad (1)$$

This dimensionless number is the product of two other dimensionless vales: the Prandtl number, which is the ratio between kinematic viscosity and thermal diffusivity, and the Grashof number, which is a ratio between buoyant and viscous forces in a flow. Lower values of Rayleigh number are indicative of laminar flow, and larger numbers signify turbulence. The transition from laminar to turbulent flow occurs between a Rayleigh number of 10^8 to 10^{10}.

Experiments have been performed in order to validate numerical models and found that it is often simpler and more efficient to numerically compute state characteristics than determine the same characteristics experimentally for low Rayleigh numbers [33]. Numerical and computational methods have been utilized to accurately predict solutions to natural convection cases for a range of Rayleigh numbers [34,35]. Many of these studies have led to Nusselt and

Rayleigh number correlations, such as ones by Markatos and Pericleous [35] and Kobus and Wadekind [36], that will be compared to the results presented herein.

The first case presented involved a 2-dimensional square domain at various Rayleigh numbers. The case performed in the present work is compared to models by Barakos et al. [34]. In the model, the Rayleigh number is adjusted by changing the characteristic length (in this case the width of the square) and Nusselt and Rayleigh number correlations are found for laminar and turbulent cases. For the present case, the Rayleigh number is adjusted by also varying the gravity level. Steady state solutions are found to create a range of laminar Rayleigh numbers for both earth- and micro-gravity cases.

Second, natural convection flow is predicted based on experiments from the Nucleate Pool Boiling Experiments [7]. The NPBX experiments analyze multiple portions of the boiling curve, including natural convection. Aktinol and Dhir [9] implemented numerical models using data from the NPBX experiments. While most of their analysis involved nucleate boiling and bubble dynamics, one case presented predicts natural convection behavior. Assumptions and material properties used by Aktinol are described and used to create the model presented in this work [8]. The researchers presented Nusselt number and Rayleigh number correlations for the natural convection range of the experiment, which are compared to results predicted in the present work using FLUENT.

Nucleate boiling

In the NPBX experiments, the primary aims were to study nucleate boiling and bubble dynamics. Using data from these experiments, Dhir and other researchers have successfully simulated the experiment results, however, these models have not been proven for a broader

variety of geometries and conditions. During the nucleate boiling portions of the NPBX, the wafer temperature was increased until nucleation occurred, then the wafer was reduced to the initial temperature until quasi steady-state conditions were present. After this, the wafer temperature was increased step by step to capture data for along the boiling curve.

The numerical model by Aktinol and Dhir [9] uses an iterative procedure and a level set method to track the liquid-vapor interface. The model is two dimensional, axisymmetric, and couples the solid substrate heater. Different simulations are performed with different initial conditions. Multiple cases are described, and all consist of a set pressure, liquid subcooling, and wall superheat. The NPBX cases have been adopted to validate the commercial model for use in predicting low gravity nucleate pool boiling.

To compare the computational simulations to those by other researchers and experimental data, a few key qualities of the flow will be examined. The main quantity of interest considered will be the wall heat flux. Heat flux is used to describe the rate at which heat is transferred per unit of area. FLUENT calculates this value based on the simulated flow characteristics and heat transfer between the hot wall and the bulk fluid next to the wall. The exact methodology for calculating heat flux is described later. The second flow characteristic that will be examined is a simple qualitative look at the bubble formation and phase change in the flow. The NPBX experiments utilized a camera attached to the outside of the tank and provide images of the flow at specific times.

1.2.3. Experimental Test Cases

As mentioned briefly in the literature review, experiments have been performed on the International Space Station by Dhir and coworkers to better increase knowledge of natural

convection and nucleate pool boiling in microgravity. These results are useful for calibrating, testing, and validating numerical simulations of low gravity boiling [7,8]. While the primary goal was to study nucleate boiling, data for the natural convection range of the boiling curve are presented, as well as values for the pressure, heat flux, and temperatures needed to create a comparable model. A more in-depth description of the experiment is provided in section.

Using nucleate pool boiling data from these experiments, Dhir and other researchers have successfully simulated the experiment results, however, the heat flux is often under-predicted. During the nucleate boiling portions of the NPBX, data was captured at each wall temperature along the boiling curve until quasi-steady conditions were reached.

2. Methods

2.1 Model Basics

The computational fluid dynamics (CFD) software utilized for the present study, FLUENT, is capable of solving the mass, momentum, and energy transport equations for a wide variety of problems. The versions of these equations found in FLUENT are listed below [12].

Conservation of mass:

$$\frac{\partial \rho}{\partial t} + \nabla \cdot (\rho \vec{v}) = S_m \tag{2}$$

Conservation of momentum:

$$\frac{\partial}{\partial t} + (\rho \vec{v}) + \nabla \cdot (\rho \vec{v} \vec{v}) = -\nabla p + \nabla \cdot (\bar{\bar{\tau}}) + \rho \vec{g} + \vec{F} \tag{3}$$

Energy Equation:

$$\frac{\partial}{\partial t}(\rho E) + \nabla \cdot \left(\vec{v}(\rho E + p)\right) = \nabla \cdot \left(k_{eff} \nabla T - \sum_q \sum_j h_{j,q} \vec{J}_{j,q} + \left(\bar{\bar{\tau}}_{eff} \cdot \vec{v}\right)\right) + S_h \tag{4}$$

where k_{eff} is effective conductivity, $\vec{J}$ is diffusion of flux species j, and subscript j,q is indicative of properties of species j in phase q.

This software uses the finite volume method and upwind differencing to discretize the governing differential equations into linearized algebraic equations. The software solves these equations using the algebraic multigrid (AMG) method.

2.1.1 Boussinesq Density Approximation and Natural Convection

The Boussinesq density approximation is a common model used in natural convection and buoyancy driven flows. The approximation was first published in 1897 by Joseph Boussinesq and has been a staple in computational fluid dynamics. In the model, density is assumed to be constant in all terms of the mass, momentum, and energy equations where gravity is not a variable. Where gravity is a variable in a term in the equation, like the momentum equation, an approximation for the actual density is used instead. Because of this, the computational time is not greatly affected. This approximation utilizes the defined constant density ρ_0, the thermal expansion coefficient β, and the difference in temperature between the area of interest and the reference temperature ΔT, which results in the following equation for density:

$$\rho = \rho_0(1 - \beta\Delta T) \tag{5}$$

The Boussinesq model cannot be used for flows with large temperature difference, combustion, calculation of species, or reacting flows [12,37]. None of these limitations are found in the research presented herein, so the Boussinesq model is applied to all cases. The model is applied in two locations: in the material properties, Boussinesq is selected from the density menu and the value for ρ_0 and β are defined, and in the operating conditions where reference

temperature is defined. For the following cases, reference temperature is the value at which the material properties are defined.

2.1.2 Discretization and Solution Methods

FLUENT allows for the user to select different solution or solving methods depending on the needs of the model. For the models herein, the pressure-based solver and SIMPLE pressure-velocity coupling scheme were utilized. When discretizing different fundamental equations, the following schemes were used: least squares cell based for gradient, body force weighted for pressure, second order upwind for momentum, geo-reconstruct for volume fraction, and second order upwind for energy. Each of these schemes was chosen based off descriptions and recommendations from the FLUENT User Guide and FLUENT Theory Guide [11,12].

2.1.3. Multiphase Models

FLUENT contains three different multiphase models for users to choose from: the Eulerian Model, the Mixture Model, and the Volume of Fluid (VOF) Model. For the presented cases, the VOF model is used. This model solves one set of momentum equations and tracks the volume fraction of each fluid within the domain. The volume fraction within each cell is a number between 0 and 1. For the work described here, 0 corresponds to only liquid in the cell, and 1 corresponds to only vapor. The volume fraction equation is a solution of the continuity equation for the volume fraction of one of the phases. The resulting equation [12] is as follows, where *l* and *x* indicate the phases:

$$\frac{1}{\rho_l}\left[\frac{\partial}{\partial t}(\alpha_l\rho_l) = \nabla\cdot(\alpha_l\rho_l\vec{v}_l) = S_{\alpha_l} + \sum_{x=1}^{n}(\dot{m}_{lx} - \dot{m}_{xl})\right] \quad (6)$$

In the VOF model, the total energy is treated as a mass-averaged variable using the following equation [12]:

$$E = \sum_{l=1}^{n} \alpha_l \rho_l E_x \Big/ \sum_{l=1}^{n} \alpha_l \rho_l \tag{7}$$

The two phases are defined when implementing the model. The VOF model was chosen over the other options for many reasons. Namely, the VOF model has become popular when simulating evaporation and bubble motion, and in the field of tank self-pressurization modeling [28]. The VOF model is selected with two phases, explicit volume fraction formulation, and sharp interface modeling.

Within the multiphase model, mass transfer mechanisms and surface tension modeling are defined. Surface tension force modeling is used with wall adhesion and a defined constant surface tension coefficient. For the evaporation-condensation model, the Lee model is the only one currently available in the software. For the present study, the Lee model is selected with a mass transfer intensity factor of 0.1 and a constant saturation temperature.

The Lee Phase Change Model [29] is governed by the vapor transport equation:

$$\frac{\partial}{\partial t}(\alpha_v \rho_v) + \nabla \bullet \left(\alpha_v \rho_v \overrightarrow{V_v}\right) = \dot{m}_{lv} - \dot{m}_{vl} \tag{8}$$

In this equation, positive mass transfer corresponds to transfer from the liquid to the vapor. With this defined, the following equation is used to describe evaporation when $T_l > T_{sat}$.

$$\dot{m}_{lv} = r_i \alpha_l \rho_l \frac{(T_l - T_{sat})}{T_{sat}} \tag{9}$$

The mass transfer intensity factor, r_i, can range from 0.1 to 1×10^7 . This factor must be tuned to the specifics of the case being simulated. For the cases performed, 0.1 was found to be the ideal r_i value.

2.1.4. Flow Property Numerical Calculations

To compare cases to other numerical simulations and experiments the wall heat flux and Nusselt number are primarily used. Nusselt number is equal to heat transfer coefficient, h, multiplied by characteristic length, L, and then divided by the thermal conductivity, k. FLUENT calculates this using a user-defined L and k, and calculated heat transfer coefficient for the surface where the value is being taken.

$$\mathrm{Nu} = \frac{hk}{L} \tag{10}$$

$$h = \frac{q}{T_{wall} - T_{bulk}} \tag{11}$$

The surface heat transfer coefficient, h, is equal to the wall heat flux divided by the difference between the wall temperature and the reference temperature. Heat flux can easily be calculated in one dimension using Fourier's law, where it is equal to the thermal conductivity multiplied by the change in temperature over distance. However, in multi-dimensional cases, the calculate of this quantity is more complex. FLUENT can compute the temperature gradient quickly and is therefore able to efficiently find the heat flux at each time step. The heat flux at a wall is then found from the following equation:

$$\mathrm{q} = -\mathrm{k}\nabla\mathrm{T} \tag{12}$$

Thermal conductivity is not always constant with respect to temperature, but for the cases presented herein it is assumed to be constant, and ∇T is the temperature gradient.

2.2 Validation Cases

For each case that is described in the following sections, there are a few key assumptions and flow properties that are consistent:

- Homogenous fluid with no particles or gas initially present
- Initial temperature is uniform in bulk fluid
- Temperature is constant and uniform across the heated or cooled surface
- Domain is perfectly insulated
- The flow is laminar
- The flow is incompressible within each phase
- The thermodynamic and physical properties of each phase are constant except for density, which uses the Boussinesq method.

Case I: 2-Dimensional Stefan Problem

The first test case to be examined is a 2-dimensional Stefan problem. This case utilizes the Boussinesq density model and analyzes laminar models for several Rayleigh numbers. The results are compared to published mathematical models, numerical simulations, and experiments.

Background

As discussed in earlier sections, Stefan problems are common boundary value problems used to validate CFD cases involving natural convection. The Stefan problem in this test case consists of a square domain with differentially heated vertical walls. The basis for this model is a series of numerical simulations performed by Barakos et al [34]. While the research basis examined the differences in laminar and turbulent models, the present work only examines the difference in

earth-gravity and low-gravity cases. Since the cases examined are expected to contain Rayleigh numbers in the laminar range, only laminar models are implemented. The goal of this phase of the research is to confirm if the model can achieve similar results to models found in the literature.

Computational Setup

The model consists of a square domain with a non-uniform mesh that is more refined as it approaches each wall. The Rayleigh number was altered by changing the scale of the model as well as the gravity level. The scale of the model is defined by a value W, which is the width of the square domain. Eight different domain sizes are analyzed. For every case, the hot and cold walls are maintained at constant temperatures of 303 K and 283 K, respectively. The two remaining walls are adiabatic, and the interior fluid is initialized at 293 K. The boundary conditions and general geometry are shown in Figure 6. Mass, momentum, and energy are computed using a segregated solver [11]. The fluid modeled is air at atmospheric pressure, with the Boussinesq approximation [37] applied for density, and all other properties assumed to be constant. Material properties for air can be found in appendix A.

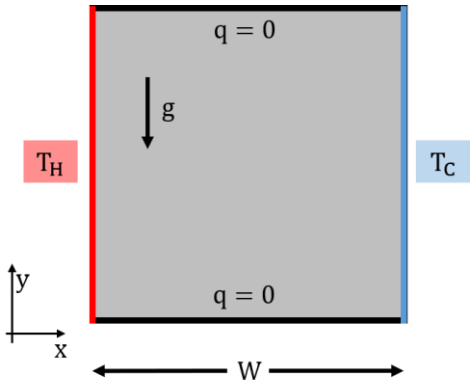

Figure 6: Natural Convection in a 2-D Square boundary conditions

A steady state solution is found for varying values of W to create a range of laminar Rayleigh numbers less than 10^6 for both the earth gravity and low gravity cases. In the low gravity cases, gravity is assumed to be approximately $g/g_e = 10^{-7}$.

Case II: 2-Dimensional Axisymmetric Natural Convection

After determining if FLUENT is accurate with low gravity natural convection cases, a case based off a 3-dimensional, micro-gravity experiment is created. This case is the first of many based off the nucleate pool boiling experiments and related simulations by Dhir et al. [7,8,38].

Background

Experiments have been performed on the International Space Station to better increase knowledge of natural convection and nucleate pool boiling in microgravity. These results are useful for calibrating, testing, and validating numerical simulations of low gravity boiling [7,8]. In this section, natural convection simulations based off experiments will be discussed.

The Nucleate Pool Boiling Experiments were performed on the International Space Station inside the Boiling Experiment Facility (BXF) during March – May of 2011 on Space Shuttle Mission STS-133. The BXF contained a diamond turned aluminum wafer that was 1 mm thick and 89.5 mm in diameter. This wafer was the boiling surface for the experiment and was heated from the backside with strain gage heaters. The wafer was placed inside the test chamber, which contained bellows to maintain a constant pressure and pumps to regulate the initial temperature before starting each test. The test chamber was filled with perfluoro-n-hexane and degassed routinely [7]. A diagram of the experimental setup is given in figure 7.

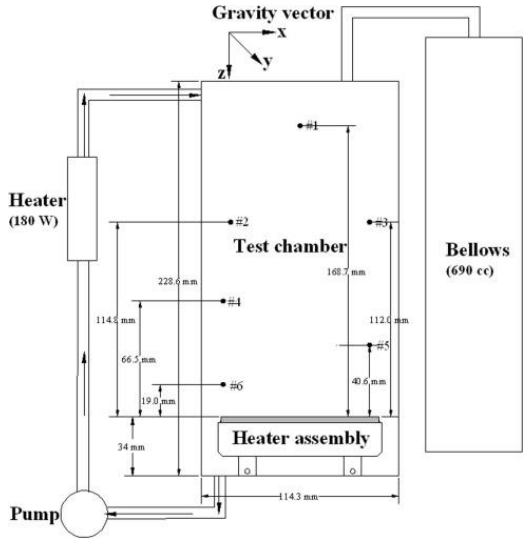

Figure 7: The Nucleate Pool Boiling Experiment test chamber [7].

Experiments were conducted to investigate the characteristics of natural convection in microgravity. Data from these experiments show a large range in Nusselt numbers, but are close to correlations by Kobus and Wadekind [36]. However, it is estimated that the time required to reach steady state for the setup is about 24,000 s based on the critical Rayleigh number and conduction layer thickness, whereas the experiments conducted on the ISS never lasted more than 1,800 s.

Nucleate pool boiling experiments were also conducted, and while the nucleate boiling data will not be analyzed in this section, data for the natural convection range of the boiling curve are presented, as well as data for the pressure, heat flux, and temperatures needed to create a comparable model. Assumptions and material properties used by Aktinol are described and used to create the model presented in this section. [8,9]. Material properties for aluminum and both liquid and vapor perfluoro-n-hexane are provided in appendix A.

Computational Setup

For the natural convection simulations, a rectangular mesh is created. This mesh is 44.75 mm by 225.6 mm and is axisymmetric as described in figure 8. There is also a 10 mm radius section to represent the bellows in the NPBX case. The model utilizes a transient solver with a time step of 1 s. A laminar viscosity model is applied since the Rayleigh number is expected to be within the laminar range. The fluid modeled inside the domain is perfluoro-n-hexane (PnH). The Boussinesq density approximation is used, and all material properties are assumed to be constant. The material fluid properties for PnH are presented in appendix.

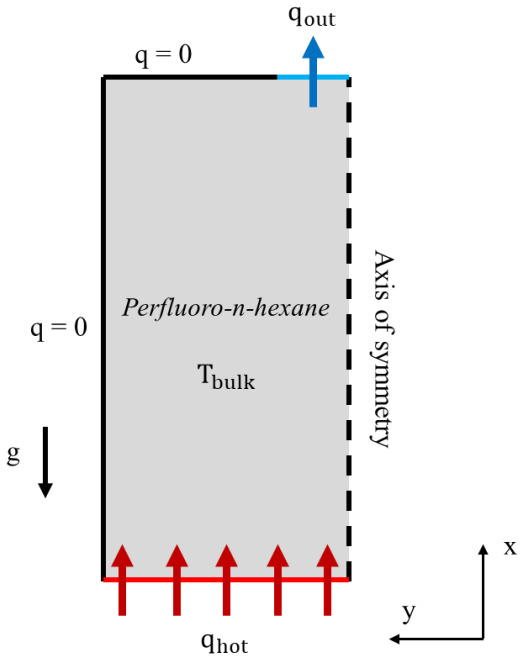

Figure 8: Domain setup and boundary conditions for the numerical model

For this case, a constant heat flux is applied at the hot wall, and an opposite heat flux adjusted for the area is applied at the outlet, which is modeled as a wall since the pressure is not expected to need an outlet since there will be no phase change. Table 1 presents the values used for heat flux, bulk temperature, saturation temperature, and pressure are given. The decision to impose a

heat flux instead of a constant temperature was made since the temperature in the experimental cases was created by using heat flux for electric heaters to get the wall to the set temperature. Another main draw to this setup was the data presentation from previous natural convection modeling attempts. The value from heat flux was chosen based off points in the natural convection range from a boiling curve recreation from the NPBX [7]. The remaining walls are all adiabatic, and an axis of symmetry exists at y = 0. Since the axis represents the vertical center of the boiling container, gravity is applied in the negative x direction. The gravitational acceleration for this case is 3.78 x 10^{-6} N/m^2. This value for gravity was chosen by researching gravitational acceleration levels found on the International Space Station during the experiments [38].

Table 1: Test matrix for validation case ii

Wall Heat Flux (W/m2)	Pressure (kPa)	T_{sat} (K)	T_{bulk} (K)
40.25	125	340.17	326.5
71.2	125	340.17	326.5
100.68	125	340.17	326.5

Nusselt number and Rayleigh number are calculated using the temperature difference between the hot wall and the average bulk fluid temperature, which is roughly equal to the initial temperature. The characteristic length, L, used is equal to the diameter of the heater divided by 4. Each case initially ran for a flow time of 1800 s to compare the result to the results from the NPBX if the fluid did not actually reach steady state. The model is then executed until the Nusselt number converges to get a more accurate comparison to established correlations by Kobus and Wadekind [36].

Case III: 3-Dimensional Nucleate Pool Boiling

Predictions of the natural convection regime of the NPBX experiments could be performed using a 2-dimensional axisymmetric domain. However, due to the 3-dimensional spherical nature of the bubbles, a 3-dimensional domain was required for simulating the nucleate pool boiling regime of the experiments.

Background

In the NPBX experiments, the primary aims of the experiments were to study nucleate boiling and bubble dynamics. Although Aktinol and Dhir have attempted to simulate the experiment, the model predictions differed by over 60% from the experiment data. The study herein focuses on determining whether the modeling capabilities in FLUENT can more accurately predict the nucleate boiling regime in the NPBX experiment. If the validation study is successful, the model could be used as a steppingstone for future work in simulating low gravity nucleate pool boiling.

Computational Setup

The 3-dimensional domain is created to model the tank and bellows in the experiment. The tank portion of the domain is a 194.6 mm tall cylinder with an 89.5 mm diameter base. Attached to the top of the cylinder is a 10 mm diameter tube connecting the tank to a smaller cylinder that is used to mimic the bellows that are used to maintain the pressure in the tank. Since density is the only property expected to change, and even so with the Boussinesq approximation is only a function of temperature, it can be assumed that the bulk pressure in the domain is constant. However, since density is expected to change, this vapor-filled space gives the liquid somewhere to expand.

Unlike the previous test case, constant temperatures are defined at the bottom of the tank and the top of the bellows section. The temperature at the base is a set wall temperature, and the saturation temperature is defined at the top. The decision to use a constant temperature on the hot wall instead of a constant heat flux was made after results from test case ii showed a large variation in wall superheat due to the longer flow time required to reach a quasi-steady state condition. The saturation temperature was chosen so that the vapor at the top will remain a vapor and will not cause any liquid at the liquid-vapor interface to evaporate. For the 3-dimensional cases, a constant temperature is used instead of heat flux. This decision was made after a more in-depth analysis of other nucleate boiling simulations and the boiling curve presented in earlier sections. All other tank and bellow walls are assumed to be perfectly insulated and have a heat flux of zero. Gravity was defined in the negative y-direction as 3.78 x 10^{-6} N/m^2. The boundary conditions for this case are presented in figure 9. Table 2 presents the boundary condition values used in the test case for both low- and earth-gravity.

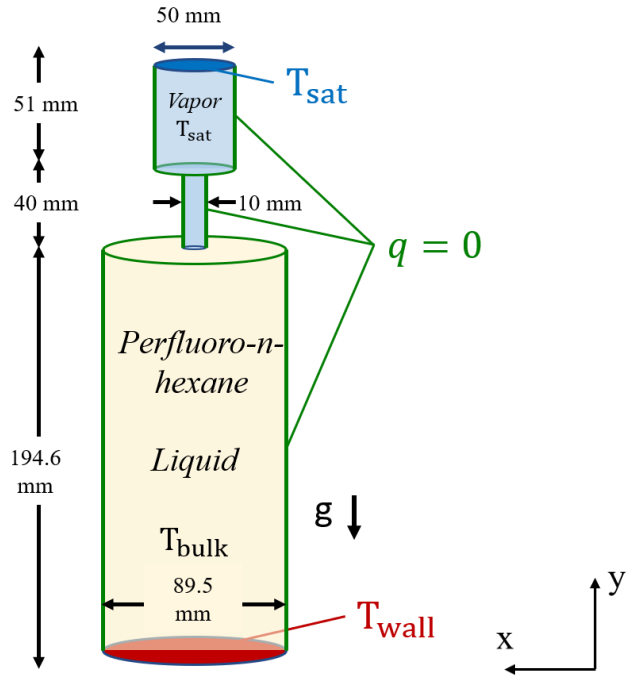

Figure 9: Boundary conditions for the 3-D NPBX Simulation

Table 2: Test matrices for validation case ii in low gravity and earth gravity

Test Cases - Low Gravity			
Wall Superheat (K)	Pressure (kPa)	T_{sat} (K)	T_{bulk} (K)
3.3	118.2	334.5	324.5
4.4	121.5	335.3	325.3
4.9	126.4	336.6	326.6
5.6	139.9	339.9	329.9

Test Cases - Earth Gravity			
Wall Superheat (K)	Pressure (kPa)	T_{sat} (K)	T_{bulk} (K)
5	128	341.0	330.5
8	128	341.0	330.5
12	128	341.0	330.5

For each test case, a transient, pressure-based solver was used. The volume-of-fluid multiphase model was applied, with the liquid and vapor phases defined. The saturation temperature of each case changed as the experimental cases had different pressures. While other computational models used the coupled level set VOF method, only the VOF method was used. The standard VOF model is less expensive computationally. In addition, the resolution of the sharp bubble interface was unnecessary in quantifying the global quantities (e.g. Nu and Ra) which were assessed for the experiments. Another property defined in the phase iteration box of the multiphase model is the surface tension coefficient. Wall adhesion was turned on in order to capture bubble formation from the hot plate.

This case also continues to use a laminar model. While nucleate boiling typically occurs in the turbulent flow regime, the points evaluated in this section occur before the critical heat flux

where a stronger turbulent flow is present. The cases here are within the laminar range based on an expected Rayleigh number less than 100 due to the low gravity magnitude.

Each case is initialized to have a liquid-filled tank and a vapor filled bellow. The values for the test cases are based on experimental data from Warrier et al. [7]. For each point, the heat flux, wall superheat, and saturation pressure is given. A range of liquid subcooling was given for the series, so the midpoint, 10 K, was chosen. For each pressure, the saturation temperature was interpolated based on experimental data from Taylor [39]. The liquid is initially at the bulk temperature, and the vapor is all at saturation temperature. The case is then run using a variable time step in order to capture the complexities of the flow. This model consists of four microgravity cases and three earth gravity cases.

3. Results

Case I: 2-Dimensional Stefan Problem

The results for Stefan cases using earth's gravity are presented in figure 10 and compare favorably with laminar correlations found by Barakos et al. [34] and Markatos and Pericleous [35]. The low gravity cases show little variation in Nusselt number for the two smallest Rayleigh number cases but begin to follow the same trend as the earth gravity cases starting in the range of $Ra = 10^2$, which is the range of the experimental data from the NPBX [7]. The characteristic length stale, L, in this case is the width of the domain, W. Nusselt Number vs. Rayleigh Number correlations are plotted in Figure along with experimental correlations found by Kobus and Wadekind [36].

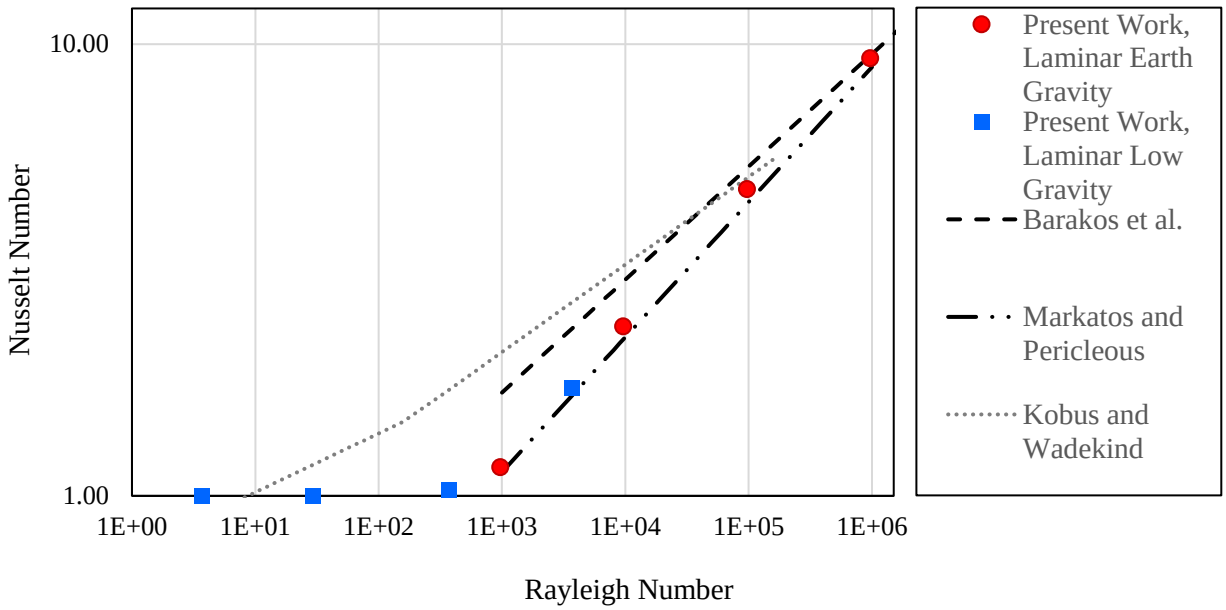

Figure 10: Rayleigh Number vs. Nusselt Number

From these results, it can be assumed that FLUENT is accurate for Rayleigh numbers less than 10^6 for earth and low gravity cases. The Nusselt number is low until around Ra = 100, which means that buoyancy driven, natural convection flow is not a significant mode of heat transfer in that range. This is expected since both numbers are used to describe flow intensity in natural convection.

Case II: 2-Dimensional Axisymmetric Natural Convection

The results from the simulations are compared to results from the NPBX [7] and numerical correlations by Kobus and Wadekind [36]. In figure 11, two sets of results are presented: one set for a flow time of 1800 s, and the second after quasi-steady state conditions were achieved, which occurred around a flow time of 100,000 s. The 1800 s results do not differ with Rayleigh number, and are slightly larger in magnitude than the highest Nusselt number found from the

experiments by the NPBX [7]. This shows that in the simulation, quasi-steady state is not reached until a much greater flow time.

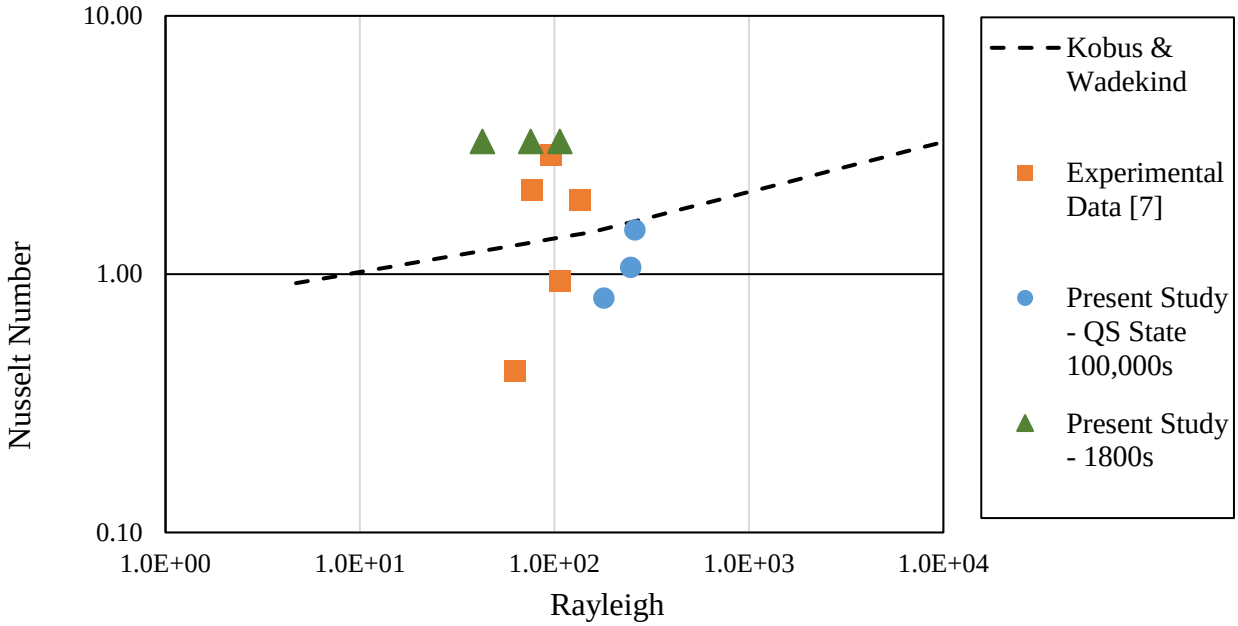

Figure 11: Low gravity dimensionless number correlations from the present numerical model at 1800 seconds of flow time and at quasi-steady state, experimental results from the NPBX [7], and an experimental correlation from Kobus and Wadekind [36]

The quasi-steady results are more accurate when it comes to Nusselt and Rayleigh number correlations, but the Rayleigh numbers are all slightly larger than the experiments. This is likely due to either a larger temperature difference between the hot wall and the bulk fluid caused by a longer heating time combined with the constant heat flux, difference in the magnitude of gravitational acceleration used to calculate Rayleigh number, or a combination of the two factors. The large difference in wall superheat is apparent in table 3 and figure 12.

Table 3: NPBX experimental [7] vs. present work simulated wall superheats

Wall Heat Flux (W/m2)	Experimental Wall Superheat (K)	Simulated Wall Superheat (K)	Percent Difference
40.25	-15.781	-8.540	46%
71.2	-10.781	-4.590	57%
100.68	-5.781	-0.820	86%

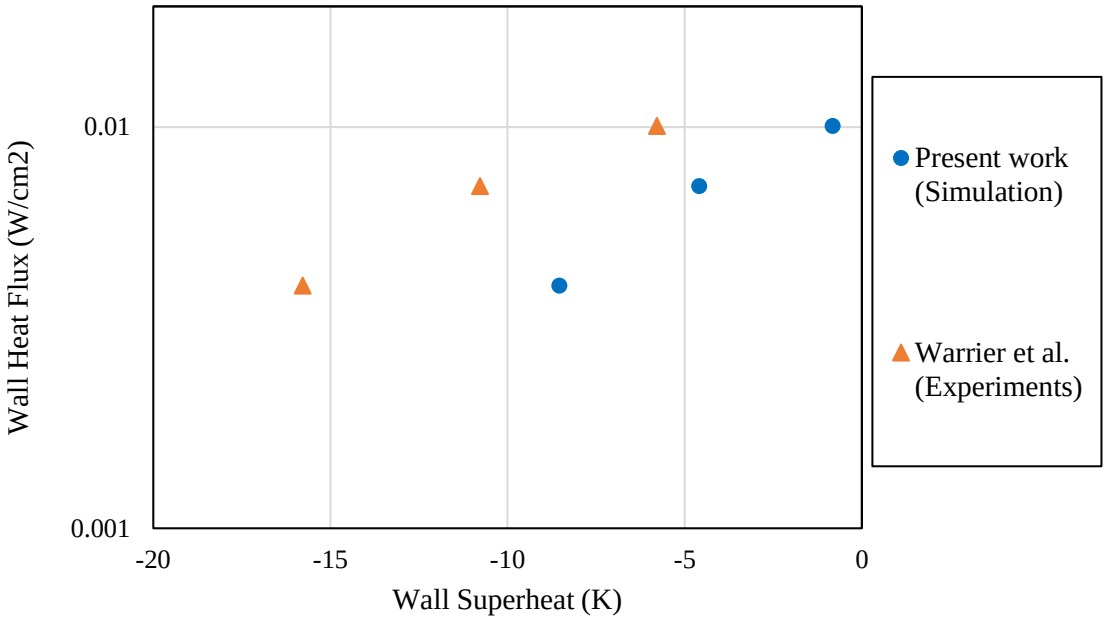

Figure 12: Wall superheat vs. wall heat flux for the present models and experimental data from the NPBX [7]

Velocity contours of the flow, shown in figure 13, demonstrate that buoyancy-driven natural convection flow is occurring in the domain. The maximum magnitude of the velocity in quasi-steady flow is 2.76×10^{-5} m/s. This shows that the commercial software can reasonably predict the flow field due to natural convection in low gravity.

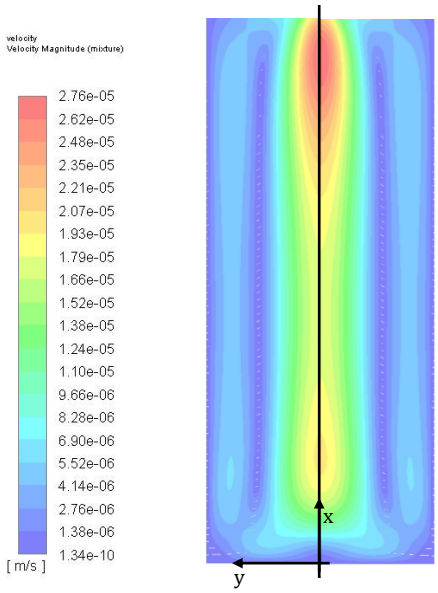

Figure 13: Velocity vectors for the domain

A mesh study was performed for the cases to determine if the solution was mesh-independent. Three different mesh cell sizes were analyzed, and the plots for Nusselt number vs. flow time are shown in figure 14. From the analysis, it can be seen that for the first 3,500 s of flow time, the results produced using each mesh are indistinguishable. However, around this time the results obtained using the less dense meshes show an increase in Nusselt number. The results obtained using the denser mesh show an increase in Nusselt number around 4,500 s. Fluctiations in the Nusselt number occur, and the solutions are not equivalent at each time step, but have a similar amplitude. For all meshes, the Nusselt number for each mesh converges at approximately 120,000 s.

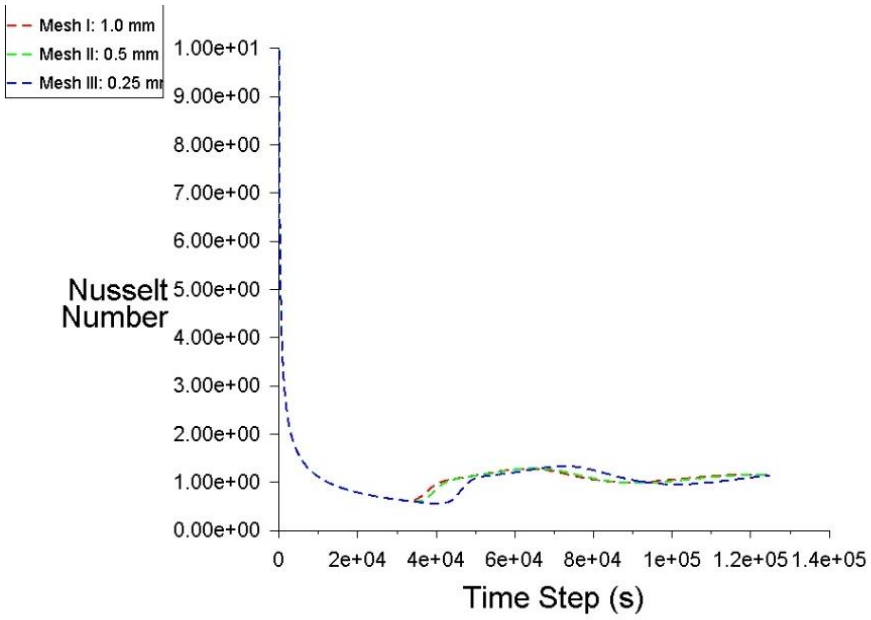

Figure 14: Nusselt number as a function of time for various mesh sizes.

Case III: 3-Dimensional Nucleate Pool Boiling

This model was quantitatively and qualitatively compared to experimental data and numerical simulations performed by Dhir and Aktinol [7,8,38], as well as other experimental data from a multitude of cases. It can be seen from table 4 and figure 15 that the present model over-predicts the heat flux and has a less-steep slope between values than the experimental and other simulated results. Another interesting point to note is that the highest wall temperature difference modeled is comparable to the experimental data.

Table 4: Results from the low gravity simulations compared to experimental data from Warrier et a. [7] and simulations by Aktinol [8].

	Experiment	Aktinol Numerical Model		Present Model	
Wall Superheat	Flux (W/cm2)	Flux (W/cm2)	Percent Difference	Flux (W/cm2)	Percent Difference
3.3 K	0.086	0.034	61%	0.368	327%
4.4 K	0.186	0.071	62%	0.402	117%
4.9 K	0.344	0.125	64%	0.531*	54%
5.6 K	0.593	0.190	68%	0.568	4%

*4.9 K results presented are only at a flow time of 60 seconds due to a late simulation start.

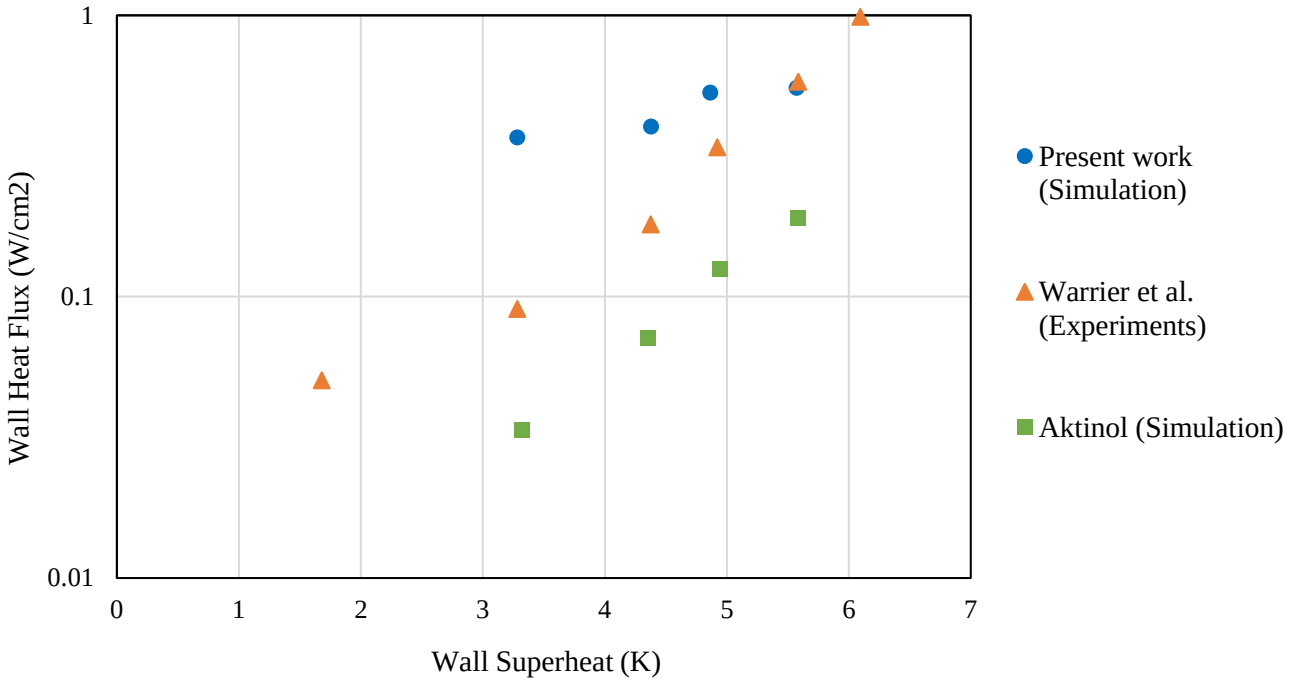

Figure 15: Heat flux vs. Wall superheat for the present work, experiments from the NPBX [7], and numerical simulations from Aktinol [8]

From analyzing the heat flux over time as shown in figure 16, the 5.6 T_{wall} case appears to be closer to a quasi-steady condition than the rest of the values, which could explain why that case has a closer value to the experimental results. The other values have not yet reached quasi-steady state, but based on current trends with heat flux, are expected to decrease in value over time and

become more like the results found experimentally. Heat flux is expected to drop in the low gravity cases due to the smaller amount of convection present when compared to earth gravity cases. Heat flux is calculated by multiplying the conductivity, which is assumed to be constant, with the temperature gradient, which is based only on the wall temperature and the wall adjacent temperature calculated at the center of the cells bordering the boundary. Since less convection is present due to the lower acceleration due to gravity, the heat will not be removed from the wall as quickly as in an earth gravity case. This results in an average wall adjacent temperature that becomes closer in magnitude to the temperature at the wall as flow time passes, which leads to a smaller temperature gradient and heat flux.

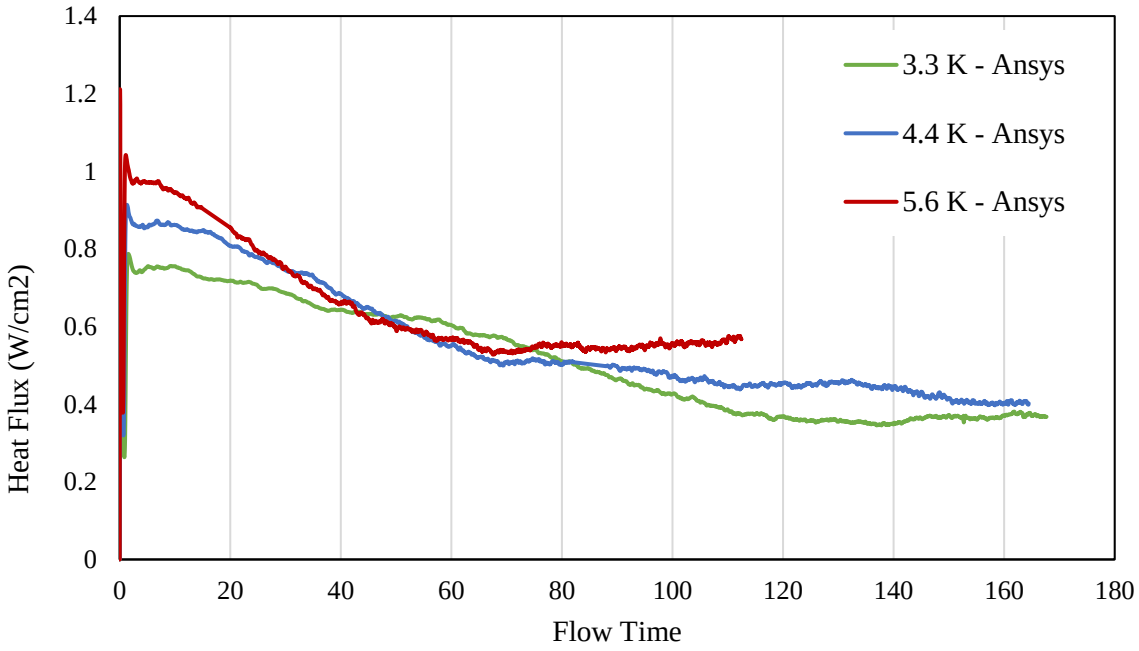

Figure 16: Heat flux vs. time for three different wall superheats in the present study

From a qualitative perspective, the simulation at the current flow time has created similar bubbles to the experiment. In the experimental pictures, there are a few small but substantial bubbles in the viewing window. The simulation has created a few bubbles around the edges of

the tank as seen in figure 17. The most compelling flow pictures occur around a flow time of 290 seconds, and at the current computational capacity and convergence speed the present simulation will take around 3 months to reach that flow time.

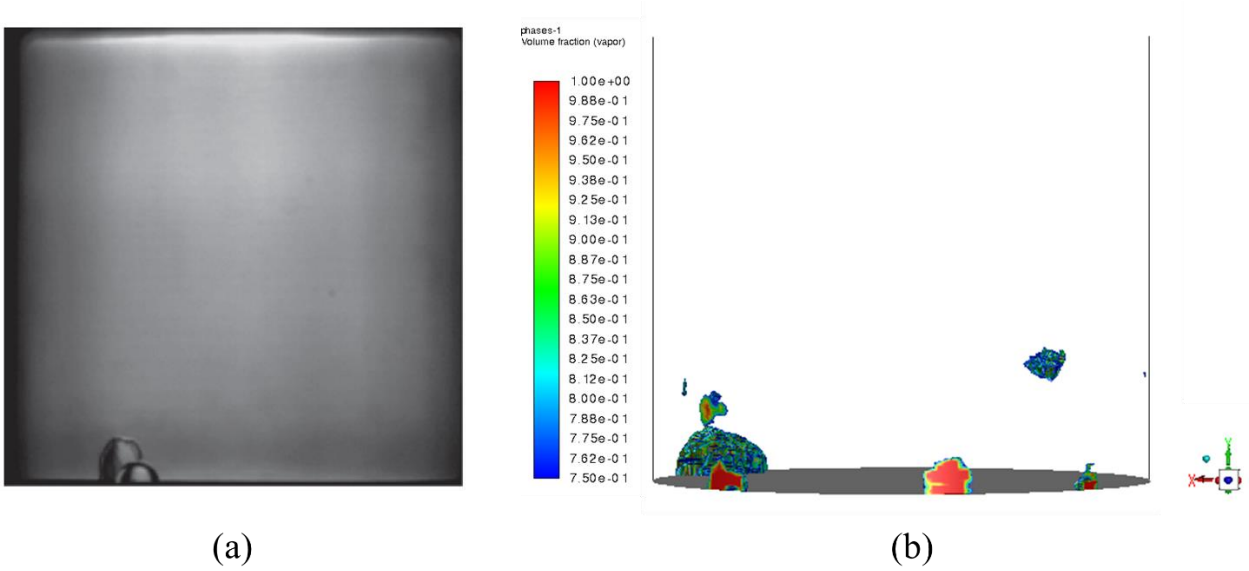

(a) (b)

Figure 17: (a) Flow visual data at 156 seconds from NPBX [7] and (b) simulated data from the present work using ANSYS FLUENT

A mesh study was performed that evaluated four different meshes of varying density. The densest mesh consisted of around 950,000 cells, while the loosest mesh had approximately 410,000 cells. Two other meshes in between were also evaluated: one with approximately 800,000 cells, and the other with 680,000 cells. Plots of the wall heat flux vs. flow time for the four meshes are shown in figure 18.

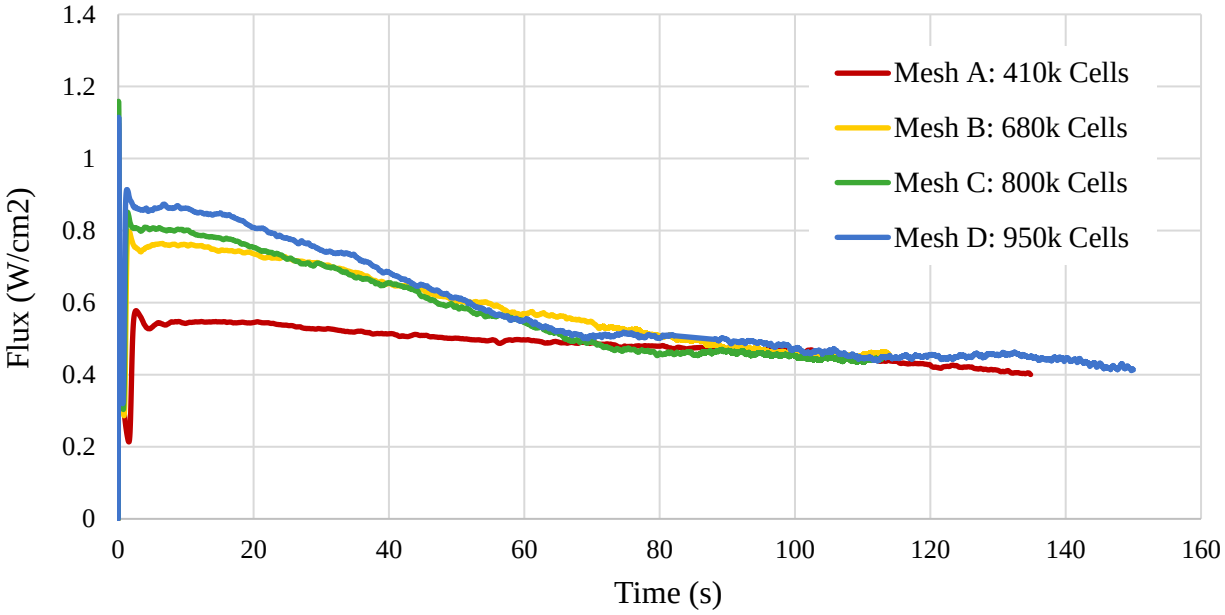

Figure 18: Mesh Study: wall heat flux vs. time

From the graph tracking heat flux with respect to flow time, each mesh begins at a different flux, but all converge and even out around 90 seconds. The wide variation between meshes until around 50-60 seconds is due to the thermal boundary layer thickness at the hot wall. The densest mesh has the smallest cell size at the wall and is able to better capture the boundary layer compared to less dense meshes. The ability for the meshes to capture activity at the wall can be seen from figure 19.

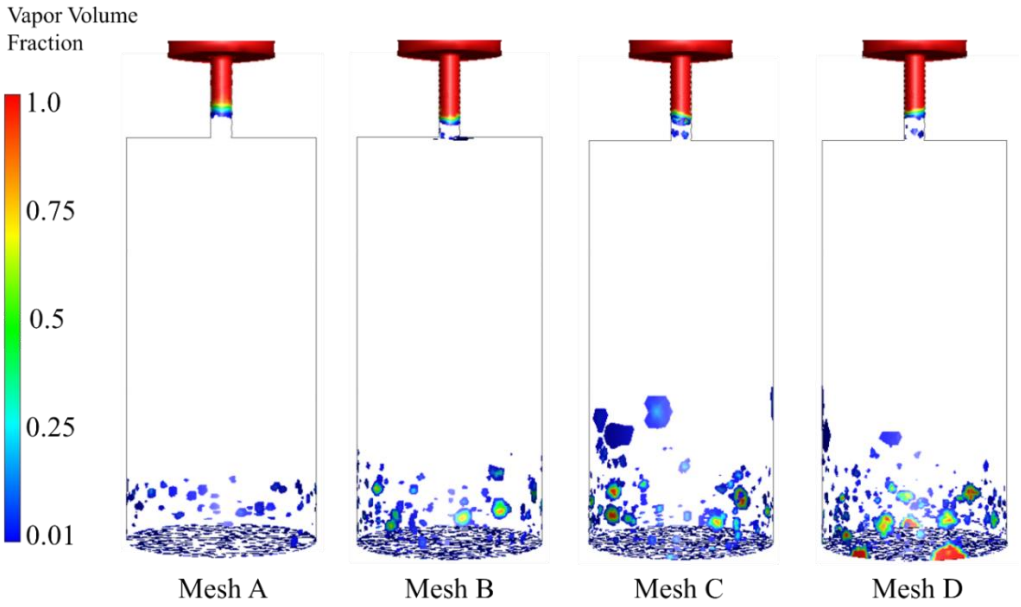

Figure 19: Vapor volume fraction contours for the four meshes at 120 seconds.

The sum of the squared residuals (RSS) for equivalent points between the meshes is displayed in table 5. This value was calculated at equivalent time steps for all four meshes. Due to slow computational calculations with mesh C, the maximum time step evaluated is 134.68 seconds. A total of 7508 time steps were used to find the RSS between each pair of meshes. The equation for RSS is as follows:

$$RSS_{A-B} = \sum_{t=0}^{t_{max}} (q_A - q_B)^2$$

Table 5: Sum squared residuals between increasing mesh sizes

Meshes	RSS
A – B (410k – 680k)	24.136
B – C (680k – 800k)	5.609
C – D (800k – 950k)	5.691

RSS_{A-B} is significantly greater than RSS_{B-C} and RSS_{C-D}. However, RSS_{C-D} is greater than RSS_{B-C}, which is not typically expected. The difference between the RSS is small, but when comparing the difference in cell number, mesh B and C are closer in size than mesh C and D, leading to the smaller RSS. After performing the mesh study, it was determined that Mesh D, consisting of approximately 950,000 cells, would be used. A mesh report is provided in appendix C. Since a variable time step was used for the cases, a time study was not performed.

Along with low-gravity cases, earth-gravity cases were also performed to see how the FLUENT model presented compares to other models and experiments. From table 6 and figure 20, it can be seen that the earth gravity heat flux predictions also have a less-steep slope than the experimental data but are underpredicted. The underprediction is most likely due to the fact that the earth gravity cases are also not at quasi-steady state. For the earth-gravity cases, heat flux is expected to rise as the simulation continues given that the stronger gravitational force will lead to more intense buoyancy driven fluid motion, which will in turn increase convective heat transfer, decrease wall adjacent temperature, and therefore heat flux. However, based on trends of heat flux over time as seen in figure 21, this does not happen. Discrepancies between the simulation and experiments are likely due to the lack of a turbulence model since the earth gravity cases have a Rayleigh number of the magnitude 10^9.

Table 6: Results from earth gravity simulations compared to experimental data [7]

Wall Superheat	Flux (W/cm2)	Flux (W/cm2)	Percent Difference
5	1.004	0.846	16%
8	1.649	1.076	35%
12	4.028	1.555	69%

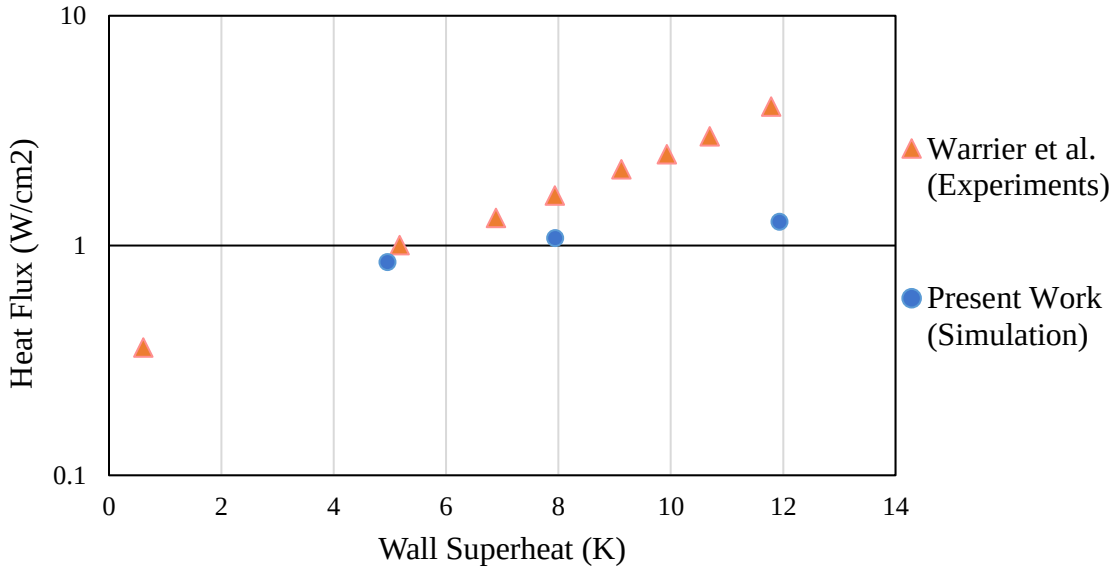

Figure 20: Earth gravity heat flux vs. wall superheat

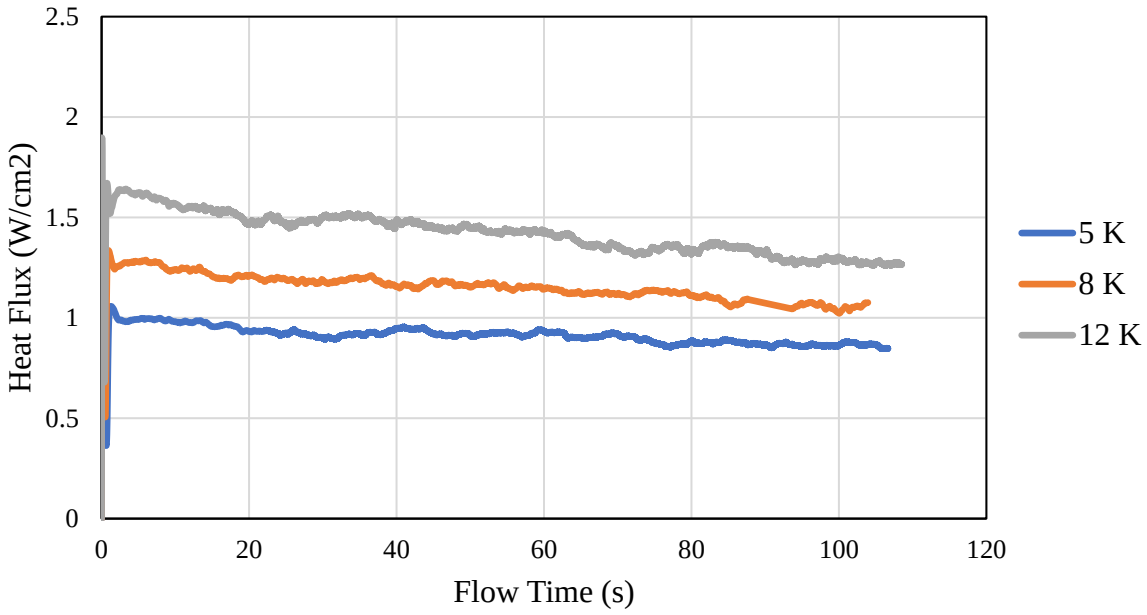

Figure 21: Earth gravity heat flux vs. flow time

4. Discussion

4.1 Computational Difficulties

The most difficult issue to navigate in the cases presented was the small time steps required to obtain converged solution based on a tolerance of 1e-3 and maximum iteration count of 2000. When the convergence criteria were first unmet, the under-relaxation factors were changed to improve convergence time. Specifically, the factor for pressure was adjusted from 0.3 to 0.25, density from 1 to 0.8, body forces from 1 to 0.8, and momentum from 0.7 to 0.5. These adjustments were successful in improving convergence, but further along in the flow time adjustments had to be made regarding time step size. At each point in the flow where convergence was not achieved, the simulation was restarted at an earlier checkpoint with a converged solution and either the maximum time step size was lowered, or the initial time step size was lowered within the variable time step scheme. The smaller maximum time step caused the simulation to run slower compared to flow time. The necessity of using small timesteps for simulations involving equations for mass, momentum, energy, and phase change is common due to the stiffness of the equations being solved. In particular, the enthalpy formulation of the energy equation which is utilized in FLUENT includes a transient pressure term which tightly couples energy to mass and momentum. The addition of the mass transfer at the interface using the Lee model only adds to the stiffness to the set of equations. In looser versions of the mesh that were not presented in the mesh study, convergence issues were often due to significant temperature gradients across large cells, but this issue was resolved by using a denser mesh.

4.2 Recommendations Future work/suggestions

Current research plans include running the simulation out to at least 300 seconds in order to see how the bubbles evolve over time. One of the largest qualitative distinguishers between microgravity and earth gravity pool boiling is the development of a single large bubble in the flow, as seen in figure 22. While present time constraints and slow computational speeds prevent this quality to be analyzed within this document, data collection and analysis will continue.

Figure 22: Experimental data from the NPBX [7] at 291 seconds

There are many opportunities for future work to continue the research. First, it may be beneficial to utilize a turbulence model for the nucleate boiling cases to compare to the existing models, especially in the earth gravity cases. The addition of turbulence may cause slower computational time but could lead to a more accurate prediction of boiling activity. There is also an option to utilize a coupled VOF and level-set multiphase method, and while it will increase the stiffness of the equations being solved, it warrants a deeper look into the mechanics of the model.

After making improvements to the microgravity nucleate boiling setup, the simulation of cryogenic fluid boiling should be evaluated and compared to experimental data and other models. This will also most likely require different tank geometries to be examined. While it is difficult to find experimental data for various tank geometries in long duration low gravity environments, a few shorter duration experiments exist involving parabolic flights and drop towers that can provide data for comparison.

5. Conclusion

While there are many opportunities for future research that can be evaluated before fully implementing this simulation software into other areas of research, from the predictions presented herein, FLUENT may have the ability to capture bubble formation and detachment in microgravity pool boiling. The software is accurate and reliable in predicting natural convection behavior in low gravity. For nucleate pool boiling, the heat flux is overpredicted using the current simulation. The addition of a turbulence model may improve the simulation predictions. The software is able to simulate the initial small bubble pool boiling behavior, but it is yet to be seen if the software can accurately capture the large singular bubble indicative of microgravity boiling. Ultimately, FLUENT may be an option for preliminary evaluation of tank design and microgravity pool boiling. The computational speed of FLUENT is not ideal, but with more computational power and time it can be a beneficial tool to quickly set up a model.

References

[1] Radebaugh, R. Cryogenics. In *The MacMillan Encyclopedia Of Chemistry*, New York, 2002.

[2] Specific Impulse. *NASA Glenn Research Center*. https://www.grc.nasa.gov/www/k-12/airplane/specimp.html. Accessed Jul. 14, 2021.

[3] Salerno, L. J., and Kittel, P. "Cryogenics and the Human Exploration of Mars." *Cryogenics*, Vol. 39, No. 4, 1999, pp. 381–388. https://doi.org/10.1016/S0011-2275(99)00043-0.

[4] SpaceX. Carbon-Fiber Propellant Tank. 2016.

[5] Dhir, V. K. "Mechanistic Prediction of Nucleate Boiling Heat Transfer–Achievable or a Hopeless Task?" *Journal of Heat Transfer*, Vol. 128, No. 1, 2006, pp. 1–12. https://doi.org/10.1115/1.2136366.

[6] Barsi, S., and Kassemi, M. "Investigation of Tank Pressurization and Pressure Control—Part II: Numerical Modeling." *Journal of Thermal Science and Engineering Applications*, Vol. 5, No. 4, 2013, p. 041006. https://doi.org/10.1115/1.4023892.

[7] Warrier, G. R., Dhir, V. K., and Chao, D. F. "Nucleate Pool Boiling EXperiment (NPBX) in Microgravity: International Space Station." *International Journal of Heat and Mass Transfer*, Vol. 83, 2015, pp. 781–798. https://doi.org/10.1016/j.ijheatmasstransfer.2014.12.054.

[8] Aktinol, E. *Numerical Simulations of Bubble Dynamics and Heat Transfer in Pool Boiling--Including the Effects of Conjugate Conduction, Level of Gravity, and Noncondensable Gas Dissolved in the Liquid*. UCLA, 2014.

[9] Aktinol, E., and Dhir, V. K. "Numerical Simulation of Nucleate Boiling Phenomenon Coupled with Thermal Response of the Solid." *Microgravity Science and Technology*, Vol. 24, No. 4, 2012, pp. 255–265. https://doi.org/10.1007/s12217-012-9308-7.

[10] *ANSYS® Fluent 19.1*. ANSYS, Inc.

[11] *ANSYS® Fluent 19.1 User Guide*. ANSYS, Inc.

[12] *ANSYS® Fluent 19.1 Theory Guide*. ANSYS, Inc.

[13] Aydelott, J. C. Normal Gravity Self-Pressurization of 9-Inch- (23 Cm) Diameter Spherical Liquid Hydrogen Tankage.

[14] Aydelott, J. C. Effect of Gravity on Self-Pressurization of Spherical Liquid-Hydrogen Tankage.

[15] Aydelott, J. C., and Spuckler, C. M. Effect of Size on Normal-Gravity Self-Pressurization of Spherical Liquid Hydrogen Tankage.

[16] Plachta, D., Christie, R. J., Jurns, J. M., and Kittel, P. "Passive ZBO Storage of Liquid Hydrogen and Liquid Oxygen Applied to Space Science Mission Concepts." *Cryogenics*, Vol. 46, Nos. 2–3, 2006, pp. 89–97. https://doi.org/10.1016/j.cryogenics.2005.11.012.

[17] Siegel, R., and Keshock, E. G. "Effects of Reduced Gravity on Nucleate Boiling Bubble Dynamics in Saturated Water." *AIChE Journal*, Vol. 10, No. 4, 1964, pp. 509–517. https://doi.org/10.1002/aic.690100419.

[18] Papell, S. S., and Faber, O. C. *Zero- and Reduced-Gravity Simulation on a Magnetic-Colloid Pool-Boiling System*. National Aeronautics and Space Administration, 1966.

[19] Kim, J. "Review of Reduced Gravity Boiling Heat Transfer: US Research." Vol. 20, No. 4, 2003, p. 8.

[20] Lee, H., Merte, Jr., H., and Chiaramonte, F. The Pool Boiling Curve in Microgravity. Presented at the 34th Aerospace Sciences Meeting and Exhibit, Reno,NV,U.S.A., 1996.

[21] Merte, Jr., H., Lee, H., and Robert Keller. *Report on Pool Boiling Experiment Prototype Model Flown on STS-47 (PBE-IA)*. Publication UM-MEAM-94-09. NASA, 1994, p. 265.

[22] Raj, R., Kim, J., and McQuillen, J. "Pool Boiling Heat Transfer on the International Space Station: Experimental Results and Model Verification." *Journal of Heat Transfer*, Vol. 134, No. 101504, 2012. https://doi.org/10.1115/1.4006846.

[23] Ryskin, G., and Leal, L. G. "Numerical Solution of Free-Boundary Problems in Fluid Mechanics. Part 2. Buoyancy-Driven Motion of a Gas Bubble through a Quiescent Liquid." *Journal of Fluid Mechanics*, Vol. 148, 1984, pp. 19–35. https://doi.org/10.1017/S0022112084002226.

[24] Sussman, M., Smereka, P., and Osher, S. "A Level Set Approach for Computing Solutions to Incompressible Two-Phase Flow." *Journal of Computational Physics*, Vol. 114, No. 1, 1994, pp. 146–159. https://doi.org/10.1006/jcph.1994.1155.

[25] Hirt, C. W., and Nichols, B. D. "Volume of Fluid (VOF) Method for the Dynamics of Free Boundaries." *Journal of Computational Physics*, Vol. 39, No. 1, 1981, pp. 201–225. https://doi.org/10.1016/0021-9991(81)90145-5.

[26] Schrage, R. W. *A Theoretical Study of Interphase Mass Transfer*. Columbia University Press, 1953.

[27] Gibou, F., Chen, L., Nguyen, D., and Banerjee, S. "A Level Set Based Sharp Interface Method for the Multiphase Incompressible Navier–Stokes Equations with Phase Change." *Journal of Computational Physics*, Vol. 222, No. 2, 2007, pp. 536–555. https://doi.org/10.1016/j.jcp.2006.07.035.

[28] Kharangate, C. R., and Mudawar, I. “Review of Computational Studies on Boiling and Condensation.” *International Journal of Heat and Mass Transfer,* Vol. 108, 2017, pp. 1164–1196. https://doi.org/10.1016/j.ijheatmasstransfer.2016.12.065.

[29] Lee, W. H. “A Pressure Iteration Scheme for Two-Phase Flow Modeling.” *Multiphase Transport: Fundamentals, Reactor Safety, Applications*, 1980, pp. 407–432.

[30] Middha, P., Ichard, M., and Arntzen, B. J. “Validation of CFD Modelling of LH2 Spread and Evaporation against Large-Scale Spill Experiments.” *International Journal of Hydrogen Energy*, Vol. 36, No. 3, 2011, pp. 2620–2627. https://doi.org/10.1016/j.ijhydene.2010.03.122.

[31] Nawaz, W., Olewski, T., and Véchot, L. “Assessment and Validation of Evaporation Models for Cryogenic Liquids.” *Process Safety and Environmental Protection*, Vol. 121, 2019, pp. 50–61. https://doi.org/10.1016/j.psep.2018.08.013.

[32] Cengel, Y. A. Chapter 10: Boiling and Condensation. In *Heat Transfer: A Practical Approach*, Mcgraw-Hill, Boston, 2002, pp. 515–560.

[33] MacGregor, R. K., and Emery, A. F. “Free Convection Through Vertical Plane Layers—Moderate and High Prandtl Number Fluids.” *Journal of Heat Transfer*, Vol. 91, No. 3, 1969, pp. 391–401. https://doi.org/10.1115/1.3580194.

[34] Barakos, G., Mitsoulis, E., and Assimacopoulos, D. “Natural Convection Flow in a Square Cavity Revisited: Laminar and Turbulent Models with Wall Functions.” *International Journal for Numerical Methods in Fluids*, Vol. 18, No. 7, 1994, pp. 695–719. https://doi.org/10.1002/fld.1650180705.

[35] Markatos, N. C., and Pericleous, K. A. “Laminar and Turbulent Natural Convection in an Enclosed Cavity.” *International Journal of Heat and Mass Transfer*, Vol. 27, No. 5, 1984, pp. 755–772. https://doi.org/10.1016/0017-9310(84)90145-5.

[36] Kobus, C. J., and Wedekind, G. L. “An Experimental Investigation into Natural Convection Heat Transfer from Horizontal Isothermal Circular Disks.” *International Journal of Heat and Mass Transfer*, Vol. 44, No. 17, 2001, pp. 3381–3384. https://doi.org/10.1016/S0017-9310(00)00330-6.

[37] Boussinesq, J. *Théorie de l’écoulement tourbillonnant et tumultueux des liquides dans les lits rectilignes a grande section*. Paris, Gauthier-Villars et fils, 1897.

[38] Dhir, V. K., Warrier, G. R., Aktinol, E., Chao, D., Eggers, J., Sheredy, W., and Booth, W. “Nucleate Pool Boiling Experiments (NPBX) on the International Space Station.” *Microgravity Science and Technology*, Vol. 24, No. 5, 2012, pp. 307–325. https://doi.org/10.1007/s12217-012-9315-8.

[39] Taylor, Jr., Z. *Equation of State of Perfluoro-n-Hexane and Isomers*. PhD Dissertaion. The University of Florida, 1966.

Appendix

A. Fluid and Material Properties

Table 7: Fluid properties for air, found in the fluid database [10]

Air Fluid Properties		
Property	Value	Units
Density	1.225	kg/m3
Specific Heat, Cp	1006.43	J/kgK
Thermal Conductivity, k	0.0242	W/mK
Viscosity	1.7894 e -05	kg/ms
Molecular Weight	28.966	kg/kmol

Table 8: Fluid properties for liquid and vapor perfluoro-n-hexane from Aktinol [8]

Perfluoro-n-hexane Fluid Properties			
Property	Liquid	Vapor	Units
Density (Boussinesq)	1592	13.4	kg/m3
Specific Heat, Cp	1102	236	J/kgK
Thermal Conductivity, k	0.0537	0.0026	W/mK
Viscosity	0.000434	1.16 e -05	Kg/ms
Molecular Weight	338	338	kg/kmol
Thermal Expansion Coefficient	0.0016	0.0016	1/K

Table 9 Material properties for aluminum, found in the fluid database [10]

Aluminum Material Properties		
Property	Value	Units
Density	2719	kg/m3
Specific Heat, Cp	871	J/kgK
Thermal Conductivity, k	202.4	W/mK

B. Natural Convection Correlations

Barakos et al. [34]

For $10^3 < Ra < 10^{11}$:

$$Nu = 0.301 \cdot Ra^{0.25}$$

Kobus and Wadekind [36]

For $300 < Ra < 10^4$:

$$Nu = 1.759 \cdot Ra^{0.13}$$

For $10^4 < Ra < 3 \times 10^7$:

$$Nu = 0.9724 \cdot Ra^{0.194}$$

Markatos and Pericleous [35]

For $10^3 < Ra < 10^6$:

$$Nu = 0.143 \cdot Ra^{0.194}$$

C. Mesh Information

Validation Case I Mesh

The following figure shows the mesh used in validation case I: the 2-dimensional Stefan problem. Mesh information is also presented.

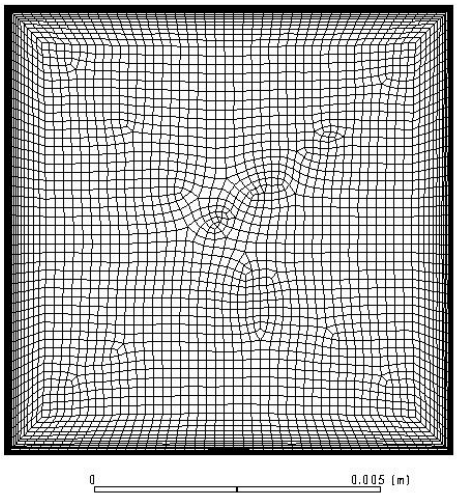

Figure 23: An example mesh used for validation case i

Minimum Orthogonal Quality = 6.76862e-01 cell 247 on zone 2 (ID: 1747 on partition: 11) at location (6.66207e-04 7.20518e-03)

Maximum Aspect Ratio = 4.35805e+01 cell 290 on zone 2 (ID: 5364 on partition: 10) at location (7.80796e-03 7.72127e-03)

Domain Extents:

- x-coordinate: min (m) = 0.000000e+00, max (m) = 7.810000e-03
- y-coordinate: min (m) = 0.000000e+00, max (m) = 7.810000e-03

Volume statistics:

- minimum volume (m3): 6.950094e-10
- maximum volume (m3): 3.559264e-08
- total volume (m3): 6.099610e-05

Face area statistics:

- minimum face area (m2): 4.074329e-06
- maximum face area (m2): 2.366603e-04

Validation Case II Mesh

Below is the mesh used in the 2-dimensional natural convection test case, case II. The mesh is most dense near the hot wall, which for this case is to the left of the mesh.

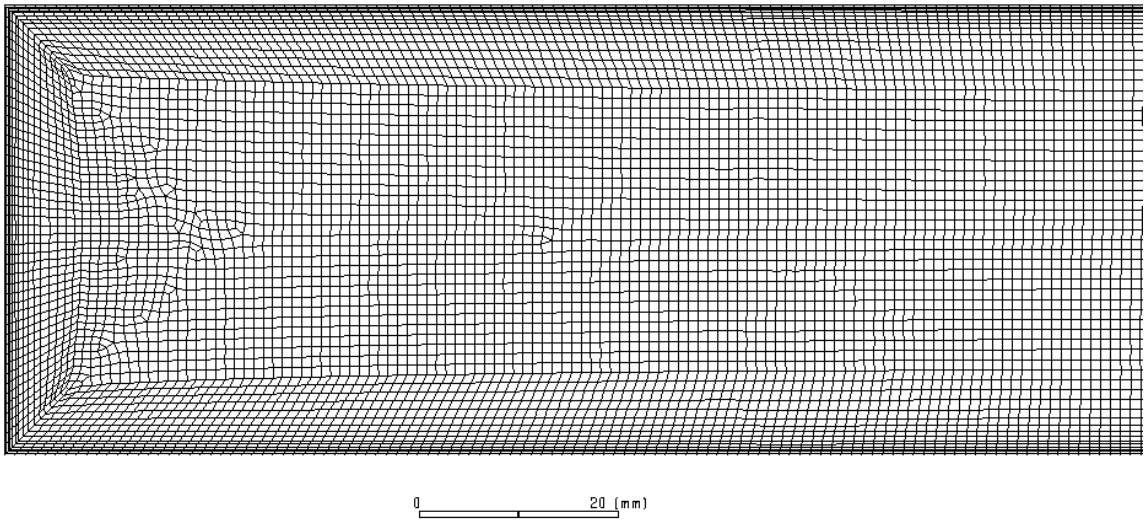

Figure 24: Zoomed in view of the section nearest the hot wall of the 2-dimensional mesh used in validation case ii

Minimum Orthogonal Quality = 9.91050e-01 cell 2990 on zone 2 (ID: 49084 on partition: 15) at location (8.96836e-04 1.22386e-04)

Maximum Aspect Ratio = 1.89990e+01 cell 3077 on zone 2 (ID: 49665 on partition: 15) at location (6.59167e-06 1.25052e-04)

Domain Extents:

- x-coordinate: min (m) = 0.000000e+00, max (m) = 1.946000e-01
- y-coordinate: min (m) = 0.000000e+00, max (m) = 1.600000e-02

Volume statistics:

- minimum volume (m3): 2.590800e-12
- maximum volume (m3): 6.384650e-09
- total volume (m3): 1.565066e-04
- minimum 2d volume (m3): 3.294666e-09
- maximum 2d volume (m3): 6.606358e-08

Face area statistics:

- minimum face area (m2): 1.317876e-05
- maximum face area (m2): 2.669745e-04

Validation Case III Meshes

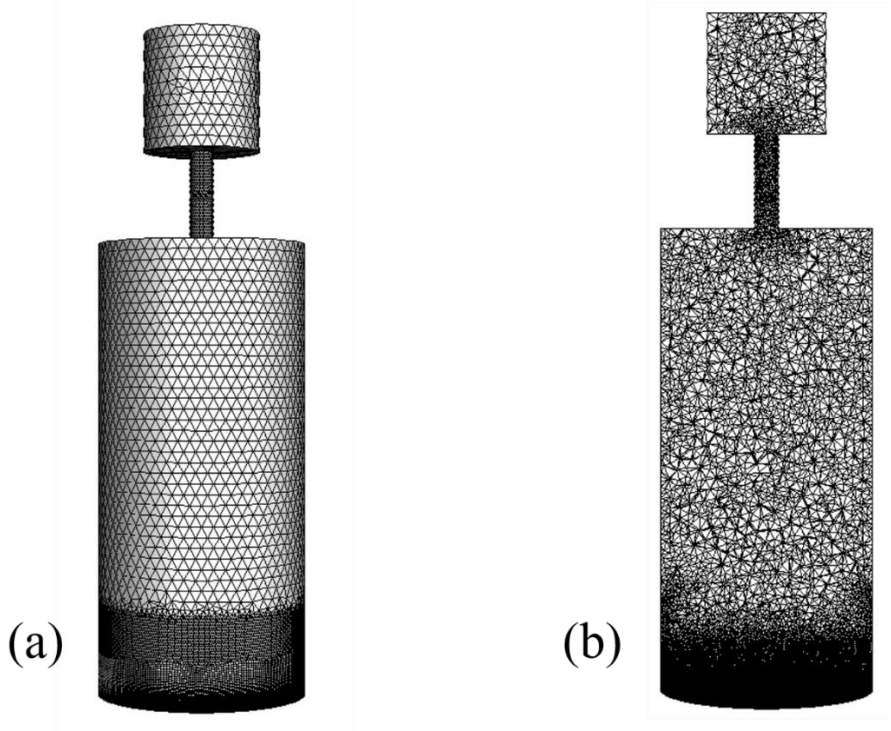

Figure 25: Mesh D used in validation case iii. (a) Views from the outside and (b) the inner x-y cross section (b) are shown.

The different meshes evaluated all have a similar appearance but have a smaller average cell volume at the hot wall to capture the boundary layer. Mesh information for all four meshes evaluated in the mesh study are presented:

Mesh A

Minimum Orthogonal Quality = 1.42301e-01 cell 3123 on zone 37 (ID: 231625 on partition: 11) at location (-3.53104e-02 5.71437e-02 2.66869e-02)

Maximum Aspect Ratio = 2.03600e+01 cell 7581 on zone 37 (ID: 5717 on partition: 2) at location (2.25516e-02 8.79517e-05 2.49068e-04)

Domain Extents:

- x-coordinate: min (m) = -4.475000e-02, max (m) = 4.475000e-02
- y-coordinate: min (m) = 0.000000e+00, max (m) = 2.856000e-01
- z-coordinate: min (m) = -4.475000e-02, max (m) = 4.475000e-02

Volume statistics:

- minimum volume (m3): 5.384694e-11
- maximum volume (m3): 3.067371e-08
- total volume (m3): 1.325600e-03

Face area statistics:

- minimum face area (m2): 1.521508e-07
- maximum face area (m2): 2.405182e-05

Mesh B

Minimum Orthogonal Quality = 1.08660e-01 cell 18422 on zone 37 (ID: 477126 on partition: 12) at location (-1.06743e-02 1.94187e-01 6.12590e-03)

Maximum Aspect Ratio = 2.31255e+01 cell 1474 on zone 37 (ID: 4093 on partition: 3) at location (-6.47157e-03 5.85464e-05 3.05694e-02)

Domain Extents:

- x-coordinate: min (m) = -4.474922e-02, max (m) = 4.475000e-02
- y-coordinate: min (m) = 0.000000e+00, max (m) = 2.856000e-01
- z-coordinate: min (m) = -4.475000e-02, max (m) = 4.475000e-02

Volume statistics:

- minimum volume (m3): 2.038830e-11
- maximum volume (m3): 3.234131e-08
- total volume (m3): 1.325593e-03

Face area statistics:

- minimum face area (m2): 7.903539e-08
- maximum face area (m2): 2.467495e-05

Mesh C

Minimum Orthogonal Quality = 1.02836e-01 cell 55604 on zone 37 (ID: 737725 on partition: 15) at location (1.18494e-03 1.94185e-01 6.95926e-03)

Maximum Aspect Ratio = 2.39377e+01 cell 8859 on zone 37 (ID: 10748 on partition: 2) at location (-1.01714e-02 5.19080e-05 -4.13014e-02)

Domain Extents:

- x-coordinate: min (m) = -4.475000e-02, max (m) = 4.475000e-02
- y-coordinate: min (m) = 0.000000e+00, max (m) = 2.856000e-01
- z-coordinate: min (m) = -4.475000e-02, max (m) = 4.475000e-02

Volume statistics:

- minimum volume (m3): 1.522780e-11
- maximum volume (m3): 3.092814e-08
- total volume (m3): 1.325582e-03

Face area statistics:

- minimum face area (m2): 6.363375e-08
- maximum face area (m2): 2.467495e-05

Mesh D

Minimum Orthogonal Quality = 1.11153e-01 cell 17767 on zone 37 (ID: 690333 on partition: 13) at location (7.47840e-04 1.94120e-01 7.11096e-03)

Maximum Aspect Ratio = 2.40147e+01 cell 37241 on zone 37 (ID: 8190 on partition: 2) at location (-4.13247e-02 4.87576e-05 -8.47974e-03)

Domain Extents:

- x-coordinate: min (m) = -4.475000e-02, max (m) = 4.475000e-02
- y-coordinate: min (m) = 0.000000e+00, max (m) = 2.856000e-01
- z-coordinate: min (m) = -4.475000e-02, max (m) = 4.475000e-02

Volume statistics:

- minimum volume (m3): 7.837812e-12
- maximum volume (m3): 3.254995e-08
- total volume (m3): 1.325569e-03

Face area statistics:

- minimum face area (m2): 5.366703e-08
- maximum face area (m2): 2.467495e-05

D. Computational Model Setup

The following points describe the specifics for the setup of the 3-dimensional nucleate pool boiling model:

General:

- Pressure based solver type
- Absolute velocity formulation
- Transient

Multiphase

- VOF
- 2 phases
- Explicit formulation
- Sharp interface modeling
- Courant number = 0.25
- Phase interactions
    - Evaporation-condensation mass transfer mechanism
        - Lee model, frequency = 0.1
        - Saturation temperature is constant
    - Surface tension
        - Surface tension force modeling
        - Wall adhesion on
        - Coefficient = 0.00835 N/m

Energy equation on

Laminar viscosity model

Cell zone conditions

- Operating conditions: temperature and pressure
- Boussinesq parameters

Methods

- Pressure-velocity coupling: simple
- Spatial discretization
    - Gradient: least squares cell based
    - Pressure: body force weighted
    - Momentum: second order upwind
    - Volume fraction: geo-reconstruct
    - Energy: second order upwind
- Transient formulation: first order implicit
- Controls
    - Pressure: 0.25
    - Density: 0.8
    - Body forces: 0.8
    - Momentum: 0.5
    - Vaporization mass: 1
    - Energy: 1